*Institute of Space and Aeronautical Science, University of Tokyo*
*Report No. 475, January 1972*

# Numerical Calculations of Some Complicated Aerodynamic Problems by a Time-dependent Finite-difference Method

*By*

Naoki HIROSE*

*Summary*: A time-dependent finite-difference method known as Fluid-in-Cell method is applied to the inviscid compressible flow problems containing such unknown discontinuities as shock wave and contact surface for the purpose of investigating the transient unsteady flow behaviour and the resulting asymptotic steady flow field as well without making any specific assumptions on the position and the strength of those discontinuities. The problems treated in the present paper are as follows: (1) supersonic flow past a circular cylinder perpendicular to the main stream, (2) supersonic flow around a flat-faced circular cylinder parallel to the main stream, and (3) supersonic flow around a flat-faced circular cylinder with a supersonic opposing jet from the nose.

The results of the present numerical calculation for cases (1) and (2) show close agreement with those of the existing theories and experiments. It is also shown that, in case (1), the method of calculation can be successfully extended to the plane polar coordinate system.

In case (3), it becomes clear that the present method of numerical calculation can produce sufficient informations to investigate the highly complicated flow field induced by the opposing jet. The effect of the governing parameters such as free stream and jet exit Mach numbers, nozzle to body radius ratio, and total pressure ratio of the jet to the free stream on the flow pattern are investigated. It is of interest to notice that two different types of the flow field appear according to the boundary conditions: the one is a steady flow field with a Mach disc in the jet stream and a bow shock similar to the one in front of a blunt body in the supersonic flow, and the other is an unsteady flow field with ever forward-moving bow shock and periodic wave pattern in the jet stream. The both types of flow field has already been observed in the experiments.

## SYMBOLS

| | |
|---|---|
| $AK$ | parameter of artificial viscosity term |
| $B$ | coefficient of artificial viscosity term |
| $C_{ps}$ | pressure coefficient at stagnation point on body |
| $C_{pj}$ | pressure coefficient at jet nozzle exit |
| $C_{pw}$ | average pressure coefficient on the front surface of body |
| $c$ | speed of sound |

* Research Engineer, Second Aerodynamics Division, National Aerospace Laboratory, 1,880 Jindaijimachi, Chōfu, Tokyo, 182. The present paper is the Doctorial thesis of the author who has conducted the study under the guidance of Prof. R. Kawamura at I.S.A.S. during the period from 1966 to 1971.

$E$ total energy per unit mass
$E_T$ total energy in the computing region
$F$ =u, v, w or E
$f$ see chapter 3.1.
$I$ specific internal energy per unit mass
$IN1$, $IN2$ total cell numbers in axial direction shown in Fig. 1
$i, j, k$ cell numbers along axial, radial and angular directions, respectively
$JETIN$, $JETJN$ total cell numbers to represent the geometry of jet nozzle shown in Fig. 1
$JN1$, $JN2$ total cell numbers in radial direction shown in Fig. 1
$M$ Mach number
$n$ time cycle number
$p$ pressure
$p_s$ pressure at stagnation point on body
$p_0$ total pressure
$q$ explicit artificial viscosity term
$R_b$ body radius
$R_{CBS}, R_{CIF}, R_{CMD}$ radius of curvatures of bow shock wave, interface and Mach disc, respectively
$R_j$ nozzle exit radius
$R_N$ numerical Reynolds number
$S$ cross-sectional area of cell
$s$ distance along body surface
$T(1)$, etc.=0 or 1 according to the flow direction at cell boundary 1
$t$ time
$u, v, w$ velocity components in axial, radial and angular directions, respectively
$V_j$ volume of cell with index j
$x, r, \phi$ Cartesian or axial, radial and angular coordinates
$\gamma$ specific heats ratio
$\Delta_s$ axial distance between bow shock wave and interface
$\delta$ stand-off distance
$\delta E_{cf}$ change of total energy in computing region due to centrifugal forces during time increment $\delta t$
$\delta M$ mass flow transported across a cell boundary
$\delta E_T$ change of total energy in computing region during time increment $\delta t$
$\delta_s, \delta_i, \delta_j$ stand-off distances of bow shock wave, interface and Mach disc, respectively
$\delta t$ time increment of difference scheme
$\delta x, \delta r, \delta\phi$ cell widths in axial, radial and angular directions, respectively
$\varepsilon_x, \varepsilon_r, \varepsilon_\phi$ coefficients of truncation error terms in each direction
$\rho$ density
$\tau$ ratio of time increment to cell width
$\tau_{CFL}$ maximum time increment ratio given by C-F-L condition

| | |
|---|---|
| $\nu$ | order of accuracy of difference scheme or index of coordinates |
| 1, 2, 3, 4 | cell boundary numbers |

SUPERSCRIPTS:

| | |
|---|---|
| $n$ | referres to value at time $t=n\delta t$ |
| $x, r, \phi$ | refer to $x$, $r$ or $\phi$ directions, respectively |
| $\sim$ | referres to intermediate value at the end of Phase I |
| $-$ | referres to the average of normal and tilde values |
| $*$ | referres to nondimensionalized value |

SUBSCRIPTS:

| | |
|---|---|
| $i, j, k$ | refer to value at cell numbers i, j, or k, respectively |
| $j$ | referres to nozzle exit condition of jet |
| $m$ | maximum cell number in each direction |
| $\infty$ | referres to free stream |

## INTRODUCTION

Recent advance of highspeed large scale digital computers made it feasible to numerically simulate complicated physical phenomena of fluid motion by replacing the basic differential equations with an appropriate finite-difference approximation or with a physical particle model representing fluid motion. Such a numerical treatment of the problem called computer experiment or computer simulation often brings us valuable informations on the interesting problems of fluid motion in which nonlinear behaviour is predominant. Analytical approach to such problems is impossible in most cases. Even if possible, a various kind of assumptions and approximations must be provided for. The same can be said for the numerical methods proposed in the past. On the other hand, in practical physical experiments an exact selection of experimental conditions is hard to realize in general and deviation of factors from the ideal conditions may bring various effects on the results and makes it difficult to interprete them correctly. Meanwhile, the computer experiment can be regarded as an idealization of the physical experiment. A better representation and understanding of physical phenomena can be obtained from it with quite a few assumptions on initial and boundary conditions and it will play an important role of guide to the analytical treatment of the problem. Numerous works have been reported not only in the field of hydrodynamics but also in a variety of fields related to fluid motion such as plasma physics, astrophysics, meteorology and oceanography [*1*], [*2*], [*3*]. From the mathematical standpoint of view most of these works are reduced to the numerical methods of the mixed initial-boundary value problems of nonlinear partial differential equations. Theory of numerical analysis of these problems, however, is not sufficient yet to be applied to practical problems in hydrodynamics [*4*]. Therefore the results of computer experiments must be carefully interpreted with mathematical and physical insight to deduce a useful conclusion from them.

In the problems of compressible fluid flow of inviscid ideal gas, discontinuities such as shock wave and contact surface are often formed in the flow field. In general, their positions, shapes and strengths are not known beforehand and determined after the solution of the whole flow field is obtained. This is the type of nonlinear interior boundary value problem of nonlinear differential equations and their analytical solution is quite limited. A typical example of this type of problem is supersonic flow around blunt body. Although a number of numercial methods have been proposed for this problem, most of them assume the shape of shock wave and apply Rankine-Hugoniot (R-H) relation across the shock wave or assume distribution of flow variables in the shock layer. These makes the algorithms of the calculation rather complicated, and moreover, when multiple shock waves or/and contact surface are present in the unsteady flow field, these methods are hard to be applied. Therefore the methods of computer experiments can be most applicable and beneficial in such problems.

Numerical treatment of discontinuities such as shock wave is difficult and a finite-difference scheme which is valid across unknown discontinuity and gives it correctly and automatically is quite desirable as the method of computer experiment. Such a scheme was first suggested by von Neumann and Richtmyer [5]. They utilized the well-known effect of dissipative mechanism on shock waves. In viscous fluid, shock wave is smeared out to form a thin layer in which flow variables such as pressure and density vary rapidly but continuously. They introduced artificial dissipative terms simpler than the real ones which have larger value at the shock into the time-dependent hydrodynamic equations of inviscid compressible fluid so as to give the shock a thickness comparable to the scale of computing mesh and yet sufficiently small compared with the scale of the whole flow field. Ludford, Polachek and Seeger [6] calculated one-dimensional viscous compressible flow involving shock propagation using finite-difference representation of unsteady hydrodynamic equations. They had to use unrealistically large value of viscosity coefficient in order to make the shock thickness comparable with the mesh width and also to eliminate oscillation behind the shock. Their results indicate that we need not to solve Navier-Stokes (N-S) equations but the finite-difference approximation of the inviscid Euler equations with von Neumann's idea of artificial viscosity gives correct relation between the flows in front of and behind the shock. Lax [7] proposed a particular difference scheme for nonlinear hyperbolic system expressed in the form of conservation laws based upon the fact that mass, momentum and energy are conserved in hydrodynamics. He obtained discontinuous numerical solutions of discontinuous initial value problems. Artificial viscosity terms are implicitly taken into account as truncation error terms in Lax's scheme.

Numerical methods such as described above are called artificial viscosity method or time-dependent finite-difference method in which the flow field including discontinuities is calculated as a finite-difference solution of initial-boundary value problem by introducing artificial viscosity either explicitly or implicitly. A number of those methods have been proposed and applied to the hydrodynamic problems.

One category of them utilizes the conservation law form. Such schemes proposed by Lax, Rusanov [*8*] and Godunov [*4*] are of first-order accuracy. Lax's scheme was applied to various aerodynamic problems including three-dimensional flow around an axisymmetric blunt body at an angle of attack [*9*], [*10*]. However, considering the characteristics such as spacewise accuracy and required computing time, the scheme is not completely satisfactory. Lax and Wendroff [*11*] proposed a second-order-accurate scheme. Several kind of variants of two-step Lax-Wendroff scheme suitable for multi-dimensional problems have been proposed [*12*], [*13*], [*14*]. Lapidus [*15*] extended the scheme to curvelinear coordinates and Thommen [*16*] applied it to N-S equations. A third-order-accurate scheme was proposed recently by Rusanov [*17*] and Burstein and Mirin [*18*].

Methods classified into another category are not based on the conservation law form but on certain elementary physical models of fluid motion. They were developed by people at Los Alamos Scientific Laboratory and known as Particle-in-Cell (PIC) method [*19*], [*20*], Particle-and-Force (PAF) method [*21*] and Fluid-in-Cell (FLIC) method [*22*]. In PIC method, the space where fluid motion takes place is subdivided into a large number of cells by Eulerian mesh fixed to observer at rest. Each one of cells is characterized by its velocity, total energy and total mass. Meanwhile, the fluid itself is represented by a large number of Lagrangean discrete mass points called particle which move through the Eulerian mesh carrying mass, momentum and total energy. PIC method demonstrates its ability especially for multi-material problems because we can assign each kind of materials to each one of particles. The method was also applied to the problems of three-dimensional flow [*23*], viscous compressible flow [*20*], rarefied gas flow [*24*] and hypervelocity impact of solid [*25*]. However, it requires a large computer memory capacity to store the coordinates of the each particles besides cell quantities and the algorithm to calculate the transport of particles becomes too complicated and time-consuming. A full analogy to the classical particle dynamic theory is adopted to represent the fluid motion in PAF method. The ability of present day computers is insufficient for both of these methods. Rich [*26*] proposed an Eulerian extension of PIC method to continuous fluid. He considered continuous fluid instead of discrete particles moving through the Eulerian mesh, thus reducing a large amount of required memory and simplifying the calculation of transport process. Later, Gentry, Martin and Daly [*22*] made some modifications to it such as the change of one of the basic flow variables from total energy to internal energy and the adoption of more sophisticated difference scheme. This method known as FLIC method was applied to the problems of shock interaction with forward-facing step and flat-faced circular cylinder by Butler [*27*].

When shock shape is simple such as the ordinary blunt body problem, it will be convinient to apply the finite-difference method only to the shock layer and to represent the shock by discontinuous R-H relation, although one of the merits of the time-dependent finite-difference method lies in that it needs no assumption concerning shock wave. Moretti [*28*] proposed such method using a difference scheme similar to Lax-Wendroff type and also Masson, Taylor and Foster [*29*]

using Godunov's scheme. This type of calculation requires less computer memory and computing time than the ordinary finite-difference methods because coarser computing mesh can be used in it.

No detailed comparison between those methods has been reported yet. Judging from our limited experiences, however, FLIC method gives fairly good space-wise accuracy with coarser computing mesh and shorter computing time than the other first-order-accurate methods. It possesses comparatively strong stability even when the initial condition differs greatly from the asymptotic steady solution. It also can be extended to multi-material problem in which different fluids coexist separated by a contact surface [*30*].

In the present paper, some of the aerodynamic problems containing highly-complicated flow field, i.e. flow field past a circular cylinder placed either normally or parallel to the supersonic free stream and flow field induced by a supersonic opposing jet from the nose of a flat-faced circular cylinder, are numerically investigated. From the above discussion the FLIC method was adopted and used throughout the calculations. The description and discussion of the method are given in chapters 1 to 3. An extension to the plane polar coordinate system of the method is also described. In the rest of the paper are presented the results of the numerical calculations and the discussions of the resulting flow phenomena.

## 1. Basic Equations

The hydrodynamic equations of motion for the two-dimensional flow of inviscid compressible fluid are written as follows

eq. of continuity

$$\frac{\partial \rho}{\partial t}+\frac{\partial(\rho u)}{\partial x}+\frac{\partial(r^{\nu}\rho v)}{r^{\nu}\partial r}=0, \tag{1-1}$$

eqs. of momentum

$$\rho\frac{\partial u}{\partial t}+\rho u\frac{\partial u}{\partial x}+\rho v\frac{\partial u}{\partial r}+\frac{\partial p}{\partial x}=0, \tag{1-2}$$

$$\rho\frac{\partial v}{\partial t}+\rho u\frac{\partial v}{\partial x}+\rho v\frac{\partial v}{\partial r}+\frac{\partial p}{\partial r}=0, \tag{1-3}$$

eq. of energy

$$\rho\frac{\partial I}{\partial t}+\rho u\frac{\partial I}{\partial x}+\rho v\frac{\partial I}{\partial r}+p\left(\frac{\partial u}{\partial x}+\frac{\partial(r^{\nu}v)}{r^{\nu}\partial r}\right)=0, \tag{1-4}$$

where $u$, $v$, $\rho$, $p$ and $I$ are the velocity components, density, pressure and specific internal energy, respectively. In the case of a plane flow, $\nu$ takes the value of 0 and $(x, r)$ are Cartesian coordinates, while in the case of an axisymmetric flow, $\nu$ takes the value of 1 and $(x, r)$ are the axisymmetric cylindrical coordinates.

In the case of plane polar coordinate system the basic equations are

eq. of continuity

$$\frac{\partial \rho}{\partial t}+\frac{\partial(r\rho v)}{r\partial r}+\frac{\partial(\rho w)}{r\partial \phi}=0, \tag{1-5}$$

eqs. of momentum

$$\rho\frac{\partial v}{\partial t}+\rho v\frac{\partial v}{\partial r}+\rho w\frac{\partial v}{r\partial \phi}-\frac{\rho w^2}{r}+\frac{\partial p}{\partial r}=0, \tag{1-6}$$

$$\rho\frac{\partial w}{\partial t}+\rho v\frac{\partial w}{\partial r}+\rho w\frac{\partial w}{r\partial \phi}+\frac{\rho vw}{r}+\frac{\partial p}{r\partial \phi}=0, \tag{1-7}$$

eq. of energy

$$\rho\frac{\partial I}{\partial t}+\rho v\frac{\partial I}{\partial r}+\rho w\frac{\partial I}{r\partial \phi}+p\left(\frac{\partial(rv)}{r\partial r}+\frac{\partial w}{r\partial \phi}\right)=0, \tag{1-8}$$

where $v$ and $w$ are the radial and angular velocity components, respectively, and $r$ and $\phi$ are the radial and angular coordinates, respectively. In the present study the fluid is considered as ideal gas. The equation of state is

$$p=(\gamma-1)\rho I, \tag{1-9}$$

where $\gamma$ is the ratio of the specific heats of the gas.

## 2. Description of the FLIC Method

### 2.1. *Finite-difference scheme in Cartesian and cylindrical coordinates*

The brief description of the calculational procedure of the method in Cartesian and cylindrial coordinates is given in this section. More details are found in Ref.22. The computing region considered is subdivided into a number of cells as shown in Fig. 1. Each cell is denoted by the indices $i$, $j$ where $i$ and $j$ represent the cell numbers in $x$ and $r$ coordinates, respectively. In cylindrical coordinates, cell $i, j$ is a rectangular torus with central radius $(j-1/2)\delta r$ and width $\delta x$ and in Cartesian coordinates the cell is a right parallelpiped. The volume $V_j$, the axial cross-sectional area $S_j^x$ and the radial cross-sectional area $S_{j+1/2}^r$ at the upper side cell boundary of cell $i, j$ are given as follows:

| | Cartesian coordinates | Cylindrical coordinates* |
|---|---|---|
| $V_j$ | $\delta x\cdot\delta r$ | $2\pi\cdot\delta x\cdot(\delta r)^2\cdot(j-1/2)$ |
| $S_j^x$ | $\delta r$ | $2\pi\cdot(\delta r)^2\cdot(j-1/2)$ |
| $S_{j+1/2}^r$ | $\delta x$ | $2\pi\cdot\delta x\cdot\delta r\cdot j$ |

* $j=1$ at the adjacent cell to the $x$ axis.

Each cell is characterized by the flow variables such as density $\rho_{ij}^n$, velocity $u_{ij}^n$, $v_{ij}^n$ and internal energy $I_{ij}^n$ where superscript $n$ represents the value at time $t=n\delta t$. When the values of flow variables at time $n\delta t$ are assigned to each cell, new values after a

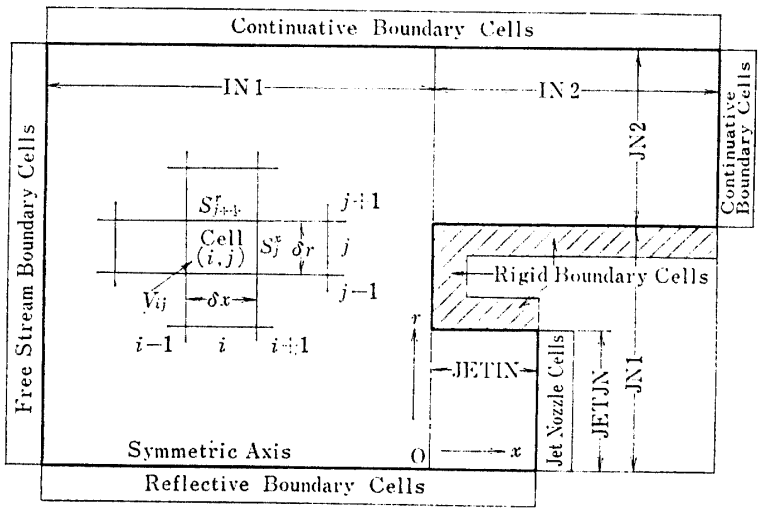


FIG. 1. Cell arrangement in Cartesian coordinates and concept of the problems (see in the text).

time increment $\delta t$ are calculated by a finite-difference approximation to the basic equations (1–1) to (1–4). This procedure consists of the following two phases in the FLIC method.

**Phase I** When transport terms are omitted and only the effects of acceleration caused by pressure gradients are taken into accounts, the basic equations (1–2) to (1–4) become

$$\rho\frac{\partial u}{\partial t}+\frac{\partial(p+q)}{\partial x}=0, \tag{2–1}$$

$$\rho\frac{\partial v}{\partial t}+\frac{\partial(p+q)}{\partial r}=0, \tag{2–2}$$

$$\rho\frac{\partial I}{\partial t}+p\left(\frac{\partial u}{\partial x}+\frac{\partial(r^{\nu}v)}{r^{\nu}\partial r}\right)+\frac{\partial(qu)}{\partial x}-u\frac{\partial q}{\partial x}+\frac{(qr^{\nu}v)}{r^{\nu}\partial r}-v\frac{\partial q}{\partial r}=0. \tag{2–3}$$

The equation of continuity is not used in Phase I because the method implicitly takes into accounts the mass conservation law in the next phase. Explicit artificial viscosity term $q$ is added to the pressure terms which prevents the instability of the difference scheme in the region where the fluid velocity is small compared with the local sound speed. The form applied here is the one proposed by Landshoff [*31*]. For example, when applied in axial direction, the term is expressed as

$$\left.\begin{aligned} q&=-Bc\rho\frac{\partial u}{\partial x}\delta x,\\ &\text{when } \frac{\partial u}{\partial x}<0 \text{ and } AK(u^2+v^2)<c^2,\\ \text{and } q&=0, \text{ otherwise,}\end{aligned}\right\} \tag{2–4}$$

where $c$ is the local sound speed, $B$ is a constant which determines the magnitude

of the artificial viscosity and $AK$ is the parameter to determine the maximum local Mach number at the cell boundary for which the artificial viscosity is applied, respectively. Explicit artificial viscosity is not applied in the regions where the fluid velocity is large compared with the local sound speed and the flow is expanding, because the truncation error terms of the finite-difference scheme play the role of artificial viscosity implicitly and these terms are sufficient to stabilize the scheme. The discussion will be given in the next chapter.

Equations (2–1) to (2–3) along with the thermodynamic equation (1–9) are approximated by the following finite-difference scheme.

$$p_{ij}^n=(\gamma-1)\rho_{ij}^n I_{ij}^n, \tag{2–5}$$

$$\tilde{u}_{ij}^n=u_{ij}^n-\frac{\delta t}{\rho_{ij}^n\delta x}\{(p+q)_{i+1/2,j}^n-(p+q)_{i-1/2,j}^n\}, \tag{2–6}$$

$$\tilde{v}_{ij}^n=v_{ij}^n-\frac{\delta t}{\rho_{ij}^n}\left\{\frac{1}{2V_j}[S_{j+1/2}^r(p_{i,j+1}^n-p_{ij}^n)-S_{j-1/2}^r(p_{i,j-1}^n-p_{ij}^n)]\right.$$
$$\left.+\frac{1}{\delta r}(q_{i,j+1/2}^n-q_{i,j-1/2}^n)\right\}, \tag{2–7}$$

$$\tilde{I}_{ij}^n=I_{ij}^n-\frac{\delta t}{\rho_{ij}^n V_j}\left\{p_{ij}^n(S_{j+1/2}^r\bar{v}_{i,j+1/2}^n-S_{j-1/2}^r\bar{v}_{i,j-1/2}^n)\right.$$
$$+\frac{1}{2}q_{i,j+1/2}^n(S_{j+1}^r\bar{v}_{i,j+1}^n+S_j^r\bar{v}_{ij}^n)-\frac{1}{2}q_{i,j-1/2}^n(S_j^r\bar{v}_{ij}^n+S_{j-1}^r\bar{v}_{i,j-1}^n)$$
$$-\bar{v}_{ij}^n S_j^r(q_{i,j+1/2}^n-q_{i,j-1/2}^n)-\bar{u}_{ij}^n S_j^x(q_{i+1/2,j}^n-q_{i-1/2,j}^n)$$
$$\left.+S_j^x[\bar{u}_{i+1/2,j}^n(p_{ij}^n+q_{i+1/2,j}^n)-\bar{u}_{i-1/2,j}^n(p_{ij}^n+q_{i-1/2,j}^n)]\right\}, \tag{2–8}$$

$$\tilde{E}_{ij}^n=\tilde{I}_{ij}^n+\frac{1}{2}\{(\tilde{u}_{ij}^n)^2+(\tilde{v}_{ij}^n)^2\}, \tag{2–9}$$

where $E$ is the total energy per unit mass and tilde $\sim$ represents the intermediate values of $u$, $v$, $I$ and $E$ at the end of Phase I. Half integer in subscripts and bar $\bar{}$ mean just as the following examples:

$$p_{i+1/2,j}^n=\frac{1}{2}(p_{ij}^n+p_{i+1,j}^n),\qquad \bar{u}_{ij}^n=\frac{1}{2}(u_{ij}^n+\tilde{u}_{ij}^n).$$

Finite-difference form of artificial viscosity term $q$ is,

$$\left.\begin{array}{c} q_{i+1/2,j}^n=-Bc_{i+1/2,j}^n\rho_{i+1/2,j}^n(u_{i+1,j}^n-u_{ij}^n), \\ \text{when } u_{i+1,j}^n-u_{ij}^n<0 \text{ and} \\ AK\{(u_{ij}^n)^2+(v_{ij}^n)^2+(u_{i+1,j}^n)^2+(v_{i+1,j}^n)^2\}<\{(c_{ij}^n)^2+(c_{i+1,j}^n)^2\}, \\ \text{and } q_{i+j,1/2}^n=0, \text{ otherwise.} \end{array}\right\} \tag{2–10}$$

Similar form is given for $q_{i,j+1/2}^n$. In the present calculation, the parameters were set as $AK=1.5$ and $B=0.3$.

**Phase II** The fluid is assumed to move across the cell boundaries with the

intermediate values of velocity and carry momentum and energy corresponding to the intermediate values of velocity and total energy of donor cell from which the fluid flows out. The final values of velocity and total energy at time $(n+1)\delta t$ are obtained by using the conservation law of mass, momentum and energy in each cell. This procedure simulates the transport effect which was neglected in Phase I.

Mass flows $\delta M^n_{i+1/2,j}$ flowing out or in through the right-side cell boundary $i+1/2$ and $\delta M^n_{i,j+1/2}$ flowing out or in through the upperside cell boundary $j+1/2$ during time increment $\delta t$ are given as,

$$\left.\begin{aligned}
\delta M^n_{i+1/2,j} &= S^x_j \rho^n_{ij} \tilde{u}^n_{i+1/2,j}\delta t, && \text{for } \tilde{u}^n_{i+1/2,j} > 0,\\
&= S^x_j \rho^n_{i+1,j} \tilde{u}^n_{i+1/2,j}\delta t, && \text{for } \tilde{u}^n_{i+1/2,j} < 0,\\
\delta M^n_{i,j+1/2} &= S^r_{j+1/2} \rho^n_{ij} \tilde{v}^n_{i,j+1/2}\delta t, && \text{for } \tilde{v}^n_{i,j+1/2} > 0,\\
&= S^r_{j+1/2} \rho^n_{i,j+1} \tilde{v}^n_{i,j+1/2}\delta t, && \text{for } \tilde{v}^n_{i,j+1/2} < 0,
\end{aligned}\right\} \qquad (2\text{–}11)$$

respectively. Summation of mass flows from all cell boundaries gives the new value of density for each cell.

$$\rho^{n+1}_{ij} = \rho^n_{ij} + \frac{1}{V_j}\{\delta M^n_{i-1/2,j} + \delta M^n_{i,j-1/2} - \delta M^n_{i+1/2,j} - \delta M^n_{i,j+1/2}\}. \qquad (2\text{–}12)$$

New values of velocity and total energy are,

$$\begin{aligned}
F^{n+1}_{ij} = \frac{1}{\rho^{n+1}_{ij} V_j}\{ & T_{ij}(1)\tilde{F}^n_{i-1,j}\delta M^n_{i-1/2,j} + T_{ij}(2)\tilde{F}^n_{i,j-1}\delta M^n_{i,j-1/2}\\
& - T_{ij}(3)\tilde{F}^n_{i+1,j}\delta M^n_{i+1/2,j} - T_{ij}(4)\tilde{F}^n_{i,j+1}\delta M^n_{i,j+1/2}\\
& + \tilde{F}^n_{ij}[\rho^n_{ij} V_j + [1 - T_{ij}(1)]\delta M^n_{i-1/2,j} + [1 - T_{ij}(2)]\delta M^n_{i,j-1/2}\\
& - [1 - T_{ij}(3)]\delta M^n_{i+1/2,j} - [1 - T_{ij}(4)]\delta M^n_{i,j+1/2}]\}, \qquad (2\text{–}13)
\end{aligned}$$

where $F$ represents either one of $u$, $v$ and $E$. Left-side boundary of cell $i\,j$ is labelled the cell boundary 1 and the rest of the cell boundaries are numbered anti-clockwise. The value of $T_{ij}(1)$ is unity when the fluid flows into the cell $i\,j$ through the cell boundary 1 and is zero when the fluid flows out through the same cell boundary.

Internal energy is finally obtained using the relation

$$I^{n+1}_{ij} = E^{n+1}_{ij} - \frac{1}{2}\{(u^{n+1}_{ij})^2 + (v^{n+1}_{ij})^2\}. \qquad (2\text{–}14)$$

The process is repeated using the final values at the previous time cycle as the initial values for the next time cycle and one can continue the processes successively as many time cycles as one wants.

### 2.2. *Formulation in plane polar coordinate system*

As far as the author knows, the extension of finite-difference scheme of FLIC or PIC method to the polar coordinate system has not been reported so far. Harlow [*32*] emphasizes that, in PIC method, Phase II must be carefully modified to take into accounts the effect of centrifugal forces and Coriolis forces on the

particle transport. His group has been working at this modification and yet have not attained the aim. In FLIC method which is an extension of PIC method to the continuum, difficulty of treatment is considerably reduced because there is no need of particle treatment. Appropriate treatment of centrifugal force terms such as $-\rho w^2/r$ and $\rho vw/r$ which appear in the equations of motion (1–6) and (1–7), however, is important in applying the basic idea of the method, i.e. the separated treatment of pressure gradient effect and transport effect to the formulation in polar coordinates. Any modification of the finite-difference scheme to include the centrifugal force terms must approximate exactly the partial differential equations (1–5) to (1–8). It can be shown that mass, momentum and energy flows across the cell boundaries in Phase II correspond to the transport terms of the basic equations in an arbitrary coordinate system and pressure gradient terms are implicitly brought into the time change portion

$$(F_{ij}^{n+1}\rho_{ij}^{n+1}-\tilde{F}_{ij}^{n}\rho_{ij}^{n})V_j \tag{2–15}$$

of the cell quantity itself of Eq. (2–13) through the procedure in Phase I. Thus the centrifugal force terms in the polar coordinates can be included in Phase I as the apparent pressure terms while Phase II is not modified basically except for the adjustment of geometrical quantities such as cell volume and cross-sectional areas. Coriolis forces need not be included because the coordinate system is not rotating in the present formulation.

The cell arrangement is shown in Fig. 2 in which the computing region is indicated by ABCD. Each cell is denoted by the indices $j$ and $k$ which represent the cell numbers in radial and angular directions, respectively. Geometrical quantities are now given as follows:

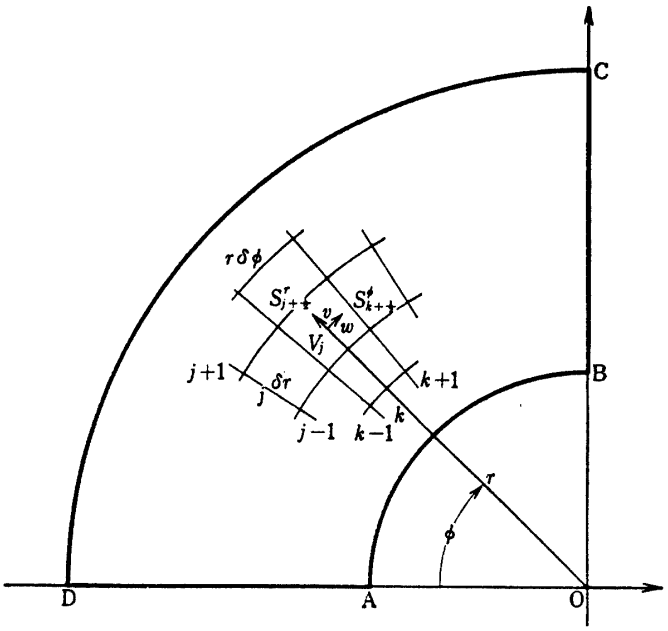


FIG. 2. Cell arrangement in plane polar coordinates.

volume $V_j = r_j \cdot \delta r \cdot \delta\phi$,

radial cross-sectional area $S^r_{j+1/2} = \left(r_j + \frac{1}{2}\delta r\right)\delta\phi$,

angular cross-sectional area $S^\phi_{k+1/2} = \delta r$,

where $\delta r$ and $\delta\phi$ are the radial and angular widths of cell respectively and $r_j$ is the radial distance of the center of cell $j\ k$ from the origin.

**Phase I** The transport terms are omitted from Eqs. (1–6) to (1–8) retaining the pressure gradient and centrifugal force terms, while the artificial viscosity terms of Landshoff type are brought in a similar manner to the previous section. Then the equations become

$$\rho\frac{\partial v}{\partial t} - \frac{\rho w^2}{r} + \frac{\partial(p+q)}{\partial r} = 0, \tag{2–16}$$

$$\rho\frac{\partial w}{\partial t} + \frac{\rho v w}{r} + \frac{\partial(p+q)}{r\partial\phi} = 0, \tag{2–17}$$

$$\rho\frac{\partial I}{\partial t} + p\left(\frac{\partial(rv)}{r\partial r} + \frac{\partial w}{r\partial\phi}\right) + \frac{\partial(qrv)}{r\partial r} - v\frac{\partial q}{\partial r} + \frac{\partial(qw)}{r\partial\phi} - w\frac{\partial q}{r\partial\phi} = 0. \tag{2–18}$$

The finite-difference approximations to these equations are

$$p^n_{jk} = (\gamma-1)\rho^n_{jk} I^n_{jk}, \tag{2–19}$$

$$\tilde{v}^n_{jk} = v^n_{jk} - \frac{\delta t}{\rho^n_{jk}}\left\{\frac{1}{2V_j}[S^r_{j+1/2}(p^n_{j+1,k} - p^n_{jk}) - S^r_{j-1/2}(p^n_{j-1,k} - p^n_{jk})] + \frac{1}{\delta r}(q^n_{j+1/2,k} - q^n_{j-1/2,k}) - \frac{1}{r_j}\rho^n_{jk}(w^n_{jk})^2\right\}, \tag{2–20}$$

$$\tilde{w}^n_{jk} = w^n_{jk} - \frac{\delta t}{r_j\rho^n_{jk}}\left\{\rho^n_{jk} v^n_{jk} w^n_{jk} + \frac{1}{\delta\phi}\left[\frac{1}{2}(p^n_{j,k+1} - p^n_{j,k-1}) + (q^n_{j,k+1/2} - q^n_{j,k-1/2})\right]\right\} \tag{2–21}$$

$$\tilde{I}^n_{jk} = I^n_{jk} - \frac{\delta t}{\rho^n_{jk} V_j}\left\{p^n_{jk}(S^r_{j+1/2}\bar{v}^n_{j+1/2,k} - S^r_{j-1/2}\bar{v}^n_{j-1/2,k}) + \frac{1}{2}q^n_{j+1/2,k}(S^r_{j+1}\bar{v}^n_{j+1,k} + S^r_j\bar{v}^n_{jk}) - \frac{1}{2}q^n_{j-1/2,k}(S^r_j\bar{v}^n_{jk} + S^r_{j-1}\bar{v}^n_{j-1,k}) - \bar{v}^n_{jk}S^r_j(q^n_{j+1/2,k} - q^n_{j-1/2,k}) - \bar{w}^n_{jk}S^\phi_k(q^n_{j,k+1/2} - q^n_{j,k-1/2}) + S^\phi_k[\bar{w}^n_{j,k+1/2}(p^n_{jk} + q^n_{j,k+1/2}) - \bar{w}^n_{j,k-1/2}(p^n_{jk} + q^n_{j,k-1/2})]\right\}, \tag{2–22}$$

$$\tilde{E}^n_{jk} = \tilde{I}^n_{jk} + \frac{1}{2}\left\{(\tilde{v}^n_{jk})^2 + (\tilde{w}^n_{jk})^2\right\}, \tag{2–23}$$

where q's are given as,

$$\left.\begin{aligned} q^n_{j+1/2,k} &= -Bc^n_{j+1/2,k}\rho^n_{j+1/2,k}(v^n_{j+1,k}-v^n_{j,k}), \\ &\text{when} v^n_{j+1,k}-v^n_{jk}<0 \text{ and} \\ AK\{(v^n_{jk})^2+(w^n_{jk})^2+(v^n_{j+1,k})^2+(w^n_{j+1,k})^2\} &< \{(c^n_{jk})^2+(c^n_{j+1,k})^2\}, \\ \text{and} \quad q^n_{j+1/2,k}&=0, \quad \text{otherwise.} \end{aligned}\right\} \quad (2\text{–}24)$$

**Phase II.** Mass flows $\delta M^n_{j+1/2,k}$ flowing out or in through the upper radial cell boundary $j+1/2$ and $\delta M^n_{j,k+1/2}$ flowing out or in through the right angular cell boundary $k+1/2$ during time increment $\delta t$ are given by

$$\left.\begin{aligned} \delta M^n_{j+1/2,k} &= S^r_{j+1/2}\rho^n_{jk}\tilde{v}^n_{j+1/2,k}\delta t, && \text{for } \tilde{v}^n_{j+1/2,k}>0, \\ &= S^r_{j+1/2}\rho^n_{j+1,k}\tilde{v}^n_{j+1/2,k}\delta t, && \text{for } \tilde{v}^n_{j+1/2,k}<0, \\ \delta M^n_{j,k+1/2} &= S^\phi_{k+1/2}\rho^n_{jk}\tilde{w}^n_{j,k+1/2}\delta t, && \text{for } \tilde{w}^n_{j,k+1/2}>0, \\ &= S^\phi_{k+1/2}\rho^n_{j,k+1}\tilde{w}^n_{j,k+1/2}\delta t, && \text{for } \tilde{w}^n_{j,k+1/2}<0, \end{aligned}\right\} \quad (2\text{–}25)$$

respectively.

New values of density, velocity and total energy are

$$\rho^{n+1}_{jk}=\rho^n_{jk}+\frac{1}{V_j}\{\delta M^n_{j-1/2,k}+\delta M^n_{j,k-1/2}-\delta M^n_{j+1/2,k}-\delta M^n_{j,k+1/2}\}, \quad (2\text{–}26)$$

$$\begin{aligned} F^{n+1}_{jk}=\frac{1}{\rho^{n+1}_{jk}V_j}\{&T_{jk}(1)\tilde{F}^n_{j-1,k}\delta M^n_{j-1/2,k}+T_{jk}(2)\tilde{F}^n_{j,k-1}\delta M^n_{j,k-1/2} \\ &-T_{jk}(3)\tilde{F}^n_{j+1,k}\delta M^n_{j+1/2,k}-T_{jk}(4)\tilde{F}^n_{j,k+1}\delta M^n_{j,k+1/2} \\ &+\tilde{F}^n_{jk}[\rho^n_{jk}V_j+[1-T_{jk}(1)]\delta M^n_{j-1/2,k}+[1-T_{jk}(2)]\delta M^n_{j,k-1/2} \\ &-[1-T_{jk}(3)]\delta M^n_{j+1/2,k}-[1-T_{jk}(4)]\delta M^n_{j,k+1/2}]\}, \end{aligned} \quad (2\text{–}27)$$

where $F$ represents either one of $v, w$ and $E$. $T_{jk}(1)$, etc. are the same as in the cylindrical coordinates. But the cell boundaries are numbered clockwise from boundary $j-1/2$ in this case.

New value of internal energy is given by

$$I^{n+1}_{jk}=E^{n+1}_{jk}-\frac{1}{2}\{(v^{n+1}_{jk})^2+(w^{n+1}_{jk})^2\}. \quad (2\text{–}28)$$

### *2.3. Initial and boundary conditions*

Besides the finite-difference scheme, the initial and boundary conditions must be specified in order to obtain a numerical solution. Initial condition is given by providing appropriate distributions of density, velocity and internal energy to every cell in the computing region at time $t=0$. If the steady solution of the flow exists, it will be determined only by the boundary condition imposed and will not depend on the initial condition. Thus, arbitrary initial distributions of the flow variables without any specific physical meaning may lead us to the asymptotic steady solution as time tends to infinity. Such setting of the initial condition may reduce the computing time as: (1) use of known approximate distributions of the flow variables, (2) assumptions of shock shape, stagnation point state on the body

surface and linear distributions of the flow variables across the shock layer, and (3) use of steady solution for different Mach number already calculated. In these cases, the asymptotic steady solution is only meaningful and time-dependent flow field during the calculation will not have any physical importance.

Another initial condition often used is the impulsive start condition in which the free stream values of the flow variables are given to every cell in the region considered. It is equivalent to the flow field induced by a body which impulsively begins to move with the free stream speed in still air. If the initial flow distribution is far different from the steady one as above, in some schemes the calculation diverges and is destroyed and the steady solution is not obtained due to nonlinear instability. Examples of the case are reported by Lapidus [*15*] and Burstein [*33*]. In the present method, however, the impulsive start condition caused no such problem and stable computation was possible.

Several kinds of boundary conditions are specified according to the setting of the problem.

**Free stream boundary:** at the upstream boundary of the computing region, fictitious boundary cells adjacent to the inner cells are assumed where the free stream values of density, velocity and internal energy are assigned to as a function of time.

**Continuative boundary:** at the down stream boundary the values of the flow variables at a fictitious boundary cell are set equal to the values at the inner cell adjacent to it. This means that the normal space derivatives are zero at the boundary and it is the zeroth order of approximation. However, any effect of boundary condition will not propagate upstream when the fluid flows out from the boundary with supersonic speed. When the flow is subsonic there, the effects of the boundary condition may propagate upstream and the whole flow field will become under the influence of them. The numerical solution may differ greatly from the exact one for such a case, so that the calculated results must be carefully analyzed and interpreted.

**Reflective boundary (rigid wall boundary):** on the body surface which coincides with cell boundary, normal mass flux and energy flux must vanish. This condition is represented by giving the values of density, internal energy and tangential velocity and the value of normal velocity with the opposite sign at the adjacent inner cell to the values at the fictitious rigid wall boundary cell inside the body surface respectively. Reflective boundary condition is also applied on the symmetric axis of the cylindrical coordinates.

When the body surface does not coincide with the cell boundary, the effective dimension of partial cell which contains a part of body surface decreases and the finite-difference scheme must be modified. The accuracy of the solution decreases in the vicinity of the body surface which is the most important region from the aerodynamic stand point of view. To avoid such deterioration of accuracy, the shape of body in the present calculation coincides with the computing mesh.

## 3. Analysis of the FLIC Method

### *3.1. The analogue differential equations*

Let us examine whether the difference scheme given in the preceding chapter consistently approximates the basic equations. When a difference scheme approximates a system of differential equations with the error of $O((\delta t)^{\nu+1})$ in the limit of time increment $\delta t \to 0$ for all sufficiently smooth solutions of the differential equations while retaining a relation between the time increment and size of cell constant, the difference scheme is $\nu$th-order-accurate. Order of accuracy $\nu$ is estimated as the order of truncation error when the Taylor expansion of the solution of the differential equations is put into the difference scheme. However, the analogue differential equations which approximate the difference scheme is more suitable for the understanding of the behaviour of the scheme. The analogue differential equations possess the identical higher order terms with the truncation error terms of the difference scheme although their sign is changed. Hereafter we shall refer "truncation error terms" as the higher order terms of the analogue differential equations.

Applying the analysis of the PIC method by Kaplan and Papetti [*34*], the FLIC analogue differential equations are derived for each of three coordinate systems. Consider a continuous function $f(x, r, t)$ which represents any one of the flow varaibles and is equal to the finite-difference solution $f_{ij}^n$ at all integer and half-integer values of subscripts. Taylor expansion of function $f$ about center of a cell i j and time $n\delta t$ is substituted into the difference scheme, then both of Phase I and II are represented by the differential equations. Combining them together, we obtain the analogue differential equations of the FLIC method for Cartesian and cylindrical coordinates,

$$\frac{\partial \rho}{\partial t}+\frac{\partial(\rho u)}{\partial x}+\frac{\partial(r^\nu \rho v)}{r^\nu \partial r}=\frac{\partial}{\partial x}\left(\varepsilon_x \frac{\partial \rho}{\partial x}\right)+\frac{\partial}{r^\nu \partial r}\left(r^\nu \varepsilon_r \frac{\partial \rho}{\partial r}\right)$$
$$-\nu\frac{(\delta r)^2}{8r}\left\{\frac{\partial^2(\rho v)}{\partial r^2}+v\frac{\partial^2 \rho}{\partial r^2}\right\}+O(\delta t), \tag{3-1}$$

$$\rho\frac{\partial u}{\partial t}+\rho u\frac{\partial u}{\partial x}+\rho v\frac{\partial u}{\partial r}+\frac{\partial p}{\partial x}=-\frac{\partial q}{\partial x}+\frac{\partial}{\partial x}\left(\rho\varepsilon_x\frac{\partial u}{\partial x}\right)+\frac{\partial}{r^\nu\partial r}\left(r^\nu\rho\varepsilon_r\frac{\partial u}{\partial r}\right)$$
$$+\varepsilon_x\frac{\partial u}{\partial x}\frac{\partial \rho}{\partial x}+\varepsilon_r\frac{\partial u}{\partial r}\frac{\partial \rho}{\partial r}-\nu\frac{(\delta r)^2}{4r}\left\{\frac{\partial u}{\partial r}\frac{\partial(\rho v)}{\partial r}+v\frac{\partial}{\partial r}\left(\rho\frac{\partial u}{\partial r}\right)\right\}+O(\delta t), \tag{3-2}$$

$$\rho\frac{\partial v}{\partial t}+\rho u\frac{\partial v}{\partial x}+\rho v\frac{\partial v}{\partial r}+\frac{\partial p}{\partial r}=-\frac{\partial q}{\partial r}+\frac{\partial}{\partial x}\left(\rho\varepsilon_x\frac{\partial v}{\partial x}\right)$$
$$+\frac{\partial}{r^\nu\partial r}\left(r^\nu\rho\varepsilon_r\frac{\partial v}{\partial r}\right)+\varepsilon_x\frac{\partial v}{\partial x}\frac{\partial \rho}{\partial x}+\varepsilon_r\frac{\partial v}{\partial r}\frac{\partial \rho}{\partial r}$$
$$-\nu\frac{(\delta r)^2}{4r}\left\{\frac{\partial v}{\partial r}\frac{\partial(\rho v)}{\partial r}+v\frac{\partial}{\partial r}\left(\rho\frac{\partial v}{\partial r}\right)+\frac{\partial^2 p}{\partial r^2}\right\}+O(\delta t), \tag{3-3}$$

$$\rho\frac{\partial I}{\partial t}+\rho u\frac{\partial I}{\partial x}+\rho v\frac{\partial I}{\partial r}+p\left\{\frac{\partial u}{\partial x}+\frac{\partial(r^{\nu}v)}{r^{\nu}\partial r}\right\}=-q\left\{\frac{\partial u}{\partial x}+\frac{\partial(r^{\nu}v)}{r^{\nu}\partial r}\right\}$$
$$+\frac{\partial}{\partial x}\left(\rho\varepsilon_x\frac{\partial I}{\partial x}\right)+\frac{\partial}{r^{\nu}\partial r}\left(r^{\nu}\rho\varepsilon_r\frac{\partial I}{\partial r}\right)+\varepsilon_x\frac{\partial\rho}{\partial x}\frac{\partial I}{\partial x}+\varepsilon_r\frac{\partial\rho}{\partial r}\frac{\partial I}{\partial r}$$
$$+\rho\varepsilon_x\left\{\left(\frac{\partial u}{\partial x}\right)^2+\left(\frac{\partial v}{\partial x}\right)^2\right\}+\rho\varepsilon_r\left\{\left(\frac{\partial u}{\partial r}\right)^2+\left(\frac{\partial v}{\partial r}\right)^2\right\}$$
$$-\nu\frac{\delta r}{2r}\left\{\frac{\partial}{\partial r}\left(\varepsilon_r\rho\frac{\partial I}{\partial r}\right)+\rho\varepsilon_r\left[\left(\frac{\partial u}{\partial x}\right)^2+\left(\frac{\partial v}{\partial r}\right)^2\right]\right.$$
$$\left.+\varepsilon_r\frac{\partial\rho}{\partial r}\frac{\partial I}{\partial r}+\delta r\frac{p}{4}\frac{\partial^2 v}{\partial r^2}\right\}+O(\delta t), \tag{3-4}$$

and for plane polar coordinates,

$$\frac{\partial\rho}{\partial t}+\frac{\partial(r\rho v)}{r\partial r}+\frac{\partial(\rho w)}{r\partial\phi}=\frac{\partial}{r\partial r}\left(r\varepsilon_r\frac{\partial\rho}{\partial r}\right)+\frac{\partial}{r\partial\phi}\left(\varepsilon_\phi\frac{\partial\rho}{\partial\phi}\right)$$
$$-\frac{(\delta r)^2}{8r}\left\{\frac{\partial^2(\rho v)}{\partial r^2}+v\frac{\partial^2\rho}{\partial r^2}\right\}+O(\delta t), \tag{3-5}$$

$$\rho\frac{\partial v}{\partial t}+\rho v\frac{\partial v}{\partial r}+\rho w\frac{\partial v}{r\partial\phi}-\frac{\rho w^2}{r}+\frac{\partial p}{\partial r}=-\frac{\partial q}{\partial r}+\frac{\partial}{r\partial r}\left(r\rho\varepsilon_r\frac{\partial v}{\partial r}\right)$$
$$+\frac{\partial}{r\partial\phi}\left(\rho\varepsilon_\phi\frac{\partial v}{\partial\phi}\right)+\varepsilon_r\frac{\partial\rho}{\partial r}\frac{\partial v}{\partial r}+\varepsilon_\phi\frac{\partial\rho}{r\partial\phi}\frac{\partial v}{\partial\phi}$$
$$-\frac{(\delta r)^2}{4r}\left\{\frac{\partial v}{\partial r}\frac{\partial(\rho v)}{\partial r}+v\frac{\partial}{\partial r}\left(\rho\frac{\partial v}{\partial r}\right)+\frac{\partial^2 p}{\partial r^2}\right\}+O(\delta t), \tag{3-6}$$

$$\rho\frac{\partial w}{\partial t}+\rho v\frac{\partial w}{\partial r}+\rho w\frac{\partial w}{r\partial\phi}+\frac{\rho vw}{r}+\frac{\partial p}{r\partial\phi}=-\frac{\partial q}{r\partial\phi}+\frac{\partial}{r\partial r}\left(r\rho\varepsilon_r\frac{\partial w}{\partial r}\right)$$
$$+\frac{\partial}{r\partial\phi}\left(\rho\varepsilon_\phi\frac{\partial w}{\partial\phi}\right)+\varepsilon_r\frac{\partial\rho}{\partial r}\frac{\partial w}{\partial r}+\varepsilon_\phi\frac{\partial\rho}{r\partial\phi}\frac{\partial w}{\partial\phi}$$
$$-\frac{(\delta r)^2}{4r}\left\{\frac{\partial w}{\partial r}\frac{\partial(\rho v)}{\partial r}+v\frac{\partial}{\partial r}\left(\rho\frac{\partial w}{\partial r}\right)\right\}+O(\delta t), \tag{3-7}$$

$$\rho\frac{\partial I}{\partial t}+\rho v\frac{\partial I}{\partial r}+\rho w\frac{\partial I}{r\partial\phi}+p\left\{\frac{\partial(rv)}{r\partial r}+\frac{\partial w}{r\partial\phi}\right\}=-q\left\{\frac{\partial(rv)}{r\partial r}+\frac{\partial w}{r\partial\phi}\right\}$$
$$+\frac{\partial}{r\partial r}\left(r\rho\varepsilon_r\frac{\partial I}{\partial r}\right)+\frac{\partial}{r\partial\phi}\left(\rho\varepsilon_\phi\frac{\partial I}{\partial\phi}\right)+\varepsilon_r\frac{\partial\rho}{\partial r}\frac{\partial I}{\partial r}+\varepsilon_\phi\frac{\partial\rho}{r\partial\phi}\frac{\partial I}{\partial\phi}$$
$$+\rho\varepsilon_r\left\{\left(\frac{\partial v}{\partial r}\right)^2+\left(\frac{\partial w}{\partial r}\right)^2\right\}+\frac{\rho\varepsilon_\phi}{r}\left\{\left(\frac{\partial v}{\partial\phi}\right)^2+\left(\frac{\partial w}{\partial\phi}\right)^2\right\}$$
$$-\frac{\delta r}{2r}\left\{\frac{\partial}{\partial r}\left(\rho\varepsilon_r\frac{\partial I}{\partial r}\right)+\varepsilon_r\frac{\partial\rho}{\partial r}\frac{\partial I}{\partial r}\right.$$
$$\left.+\rho\varepsilon_r\left[\left(\frac{\partial v}{\partial r}\right)^2+\left(\frac{\partial w}{\partial r}\right)^2\right]+\delta r\frac{p}{4}\frac{\partial^2 v}{\partial r^2}\right\}+O(\delta t), \tag{3-8}$$

where

$$\varepsilon_x=\frac{1}{2}|u|\,\delta x,\quad \varepsilon_r=\frac{1}{2}|v|\,\delta r,\quad \varepsilon_\phi=\frac{1}{2}|w|\,\delta\phi, \tag{3-9}$$

and the explicit artificial viscosity $q$ has different form according to the direction of derivatives as mentioned before.

The left-hand side of those equations is exactly the same as that of the basic equations (1–1) to (1–8). The right-hand side is the artificial viscosity and the truncation error terms. Because the $O(\delta t)$ terms have complicated forms and their effect can be included in the $O(\delta x)$ terms, they are not given explicitly here. It is clear that each term in the right-hand side vanishes if $\delta t$ goes to zero in such a way that $\tau=\delta t/\delta x$ is constant. The difference scheme satisfies the consistency condition with the first order of accuracy.

Some of the truncation error terms are similar to viscous force, thermal conduction and viscous dissipation terms in the viscous hydrodynamic equations and they introduce an artificial dissipative mechanism which makes the finite-difference calculation possible without any assumptions on shock wave and contact surface. They smooth the profiles of the flow variables at the discontinuities. However the diffusion coefficients such as $\varepsilon_x$ which may correspond to the coefficients of viscosity and thermal conductivity of real fluid depend on the size of cell and local velocity and are not invariant with the coordinate transformation. The form of these terms also depends on the difference scheme. Therefore we cannot directly relate the analogue differential equations to N-S equations. For example, if cell boundary values are used in Phase II calculation instead of the donor cell method used in the present formulation, the $O(\delta x)$ terms are all dropped. Density diffusion terms are not present in Rich's and PIC methods. But in such schemes, nonlinear instability arises in some kind of problems even if large explicit artificial viscosity terms are added to the schemes. We conjecture that the presence of diffusion terms in the equation of continuity makes the FLIC method more stable in the region of rapid change of the flow variables than the other methods.

The second-order terms with the form of $(\delta r)^2/r$ may not be neglected in the region where radius $r$ is small and are retained in the equations. However, only the region $\delta r/r\ll 1$ is considered in the calculation in the polar coordinates and the cell location is arranged to avoid the symmetric axis in the cylindrical coordinates. So these terms become at most comparable with the first-order terms even when $r$ is nearly equal to $\delta r$. Therefore they will not have any significant effect on the calculation.

### *3.2. Stability condition*

A finite-difference solution not necessarily gives an approximation to the differential solution even if the consistency condition is satisfied as pointed out by Courant, Friedrichs and Lewy [*35*]. Some kind of requirement is necessary for a finite-difference solution to coincide with the exact differential solution. The rigorous theoretical analysis was developed for the linear difference equations with

constant coefficients. The hydrodynamic equations, however, are nonlinear equations with variable coefficients and so are the corresponding difference equations. And there is no rigorous theory yet for these problems. Therefore, in practice the local stability of the linearized equations is checked [4]. A small perturbation is superposed on a smooth difference solution and put into the difference equations. Dropping the higher-order terms, the linear difference equations with coefficients which depend on the unperturbed solution is obtained. The coefficients can be regarded as constants at a fixed point on the mesh. Then the local stability is analyzed. Although the local stability condition is not always sufficient nor necessary for the overall stability of the original difference equations and such examples are pointed out by numerical analysists, von Neumann's condition for the local linearized stability gives reasonable criterion in practical problems. Local linearization seems to be justified because the instability appears locally at first for most cases.

As for the stability condition of the FLIC method, the truncation error terms with $\varepsilon_x$, etc. are brought into the analogue differential equations in Phase II treatment and they play the role of diffusion terms and increase the stability. So the stability of Phase I is investigated in this section. We take up the plane polar FLIC method proposed in the present paper for example. We assume a nearly steady flow in the vicinity of stagnation point. The distribution of the flow variables is assumed to be smooth and depend on radius only. Then it can be shown that the local linearized difference equations are reduced to the same form as that for Cartesian coordinates if a region is considered where radius $r$ is sufficiently larger than the radial cell width $\delta r$. Amplification matrix and its eigenvalues were obtained by substituting the Fourier components of the solution into the equations. von Neumann's condition requires all of the absolute eigenvalues not greater than unity. The calculation gives the stability condition for Phase I,

$$\frac{c_0 \delta t}{\delta r} \leq \min\left(\frac{1}{B}, \frac{\gamma B}{(\gamma-1)}\right), \tag{3-10}$$

where $c_0$ is the local sound speed and $B$ is the coefficient of the artificial viscosity $q$, respectively. From this criterion the difference scheme becomes unconditionally unstable when the artificail viscosity is not applied. The result of one-dimensional shock tube problem shows that when $B$ is zero, the instability appears at stagnant region behind the reflected shock wave, because the velocity is nearly zero there and the truncation error terms become too small and the computation is destroyed. The instability, however, is bounded sometimes due to the nonlinear suppression effect by the truncation error terms. In practice the stability condition will be given empirically to satisfy Courant-Friedrichs-Lewy condition,

$$c\delta t/\delta r \leq 1, \tag{3-11}$$

and another one,

$$v_{\max}\delta t/\delta r \leq 1, \tag{3-12}$$

which forbids the fluid to move over one cell width during time increment $\delta t$ because the difference schemes express no more than the relation between the adjoining cells. Here $v_{\max}$ is the maximum velocity.

The above discussion is also applicable to the other coordinates and the stability condition must not be violated anywhere in the computing region.

### *3.3. Conservation of mass and energy*

Although the FLIC method is not derived from the conservation law form of the basic equations, the conservation of mass, momentum and energy, however, must hold in the difference schemes. We will discuss the conservation of mass and energy. Momentum is not conserved in the polar and cylindrical coordinates and is omitted from the discussion.

#### *3.3.1. Mass and energy conservation in Phase I*

Density is considered to be constant during Phase I, therefore the total mass in the computing region does not change in Phase I. Total energy $E_T^n$ in the computing region at the beginning of the phase is given as

$$E_T^n=\sum_{jk}\left\{I_{jk}^n+\frac{1}{2}[(v_{jk}^n)^2+(w_{jk}^n)^2]\right\}\rho_{jk}^n V_j, \tag{3–13}$$

in the polar coordinates. At the end of Phase I, total energy becomes

$$\tilde{E}_T^n=\sum_{jk}\left\{\tilde{I}_{jk}^n+\frac{1}{2}[(\tilde{v}_{jk}^n)^2+(\tilde{w}_{jk}^n)^2]\right\}\rho_{jk}^n V_j. \tag{3–14}$$

The difference $\delta\tilde{E}_T^n$ between them is expressed as follows

$$\delta\tilde{E}_T^n=\tilde{E}_T^n-E_T^n=\sum_{jk}\rho_{jk}^n V_j\{(\tilde{I}_{jk}^n-I_{jk}^n)+\bar{v}_{jk}^n(\tilde{v}_{jk}^n-v_{jk}^n)+\bar{w}_{jk}^n(\tilde{w}_{jk}^n-w_{jk}^n)\}. \tag{3–15}$$

Substituting the equations (2–20) to (2–22) into the right-hand side of the equations and rearranging the terms to cancell with each other between the adjoining internal cells, the equation (3–15) is reduced to

$$\begin{aligned}\delta\tilde{E}_T^n=&-\delta t\sum_k\left\{\frac{1}{2}S_{j_m+1/2}^r(p_{j_m,k}^n\bar{v}_{j_m+1,k}^n+p_{j_m+1,k}^n\bar{v}_{j_m,k}^n)\right.\\&+\frac{1}{2}q_{j_m+1/2,k}^n(S_{j_m+1}^r\bar{v}_{j_m+1,k}^n+S_{j_m}^r\bar{v}_{j_m,k}^n)\\&\left.-\frac{1}{2}S_{1/2}^r(p_{1,k}^n\bar{v}_{0,k}^n+p_{0,k}^n\bar{v}_{1,k}^n)-\frac{1}{2}q_{1/2,k}^n(S_1^r\bar{v}_{1,k}^n+S_0^r\bar{v}_{0,k}^n)\right\}\\&-\delta t\sum_j\left\{\frac{1}{2}S_k^\phi(p_{j,k_m}^n\bar{w}_{j,k_m+1}^n+p_{j,k_m+1}^n\bar{w}_{j,k_m}^n)+q_{j,k_m+1/2}^n\bar{w}_{j,k_m+1/2}^n\right.\\&\left.-\frac{1}{2}S_k^\phi(p_{j,0}^n\bar{w}_{j,1}^n+p_{j,1}^n\bar{w}_{j,0}^n)-q_{j,1/2}^n\bar{w}_{j,1/2}^n\right\}+\delta\tilde{E}_{cf}^n,\end{aligned} \tag{3–16}$$

where $j=1/2$, $j_m+1/2$ and $k=1/2$, $k_m+1/2$ are the external boundaries of the

computing region, respectively. $j_m+1$ and $k_m+1$ indicate the fictitious boundary cells placed adjacent to the internal cells.

The summation of the first bracket of the equation (3–16) is the net radial energy flux through the radial boundaries of the computing region and similarly that of the second bracket is the angular energy flux through the angular boundaries. For the total energy of the system to be conserved exactly, the values at the boundary cells must be specified so that the radial energy flux given above may be equal to the corresponding value

$$\sum_k S^r_{j_m+1/2} p^n_{j_m+1/2,k} \bar{v}^n_{j_m+1/2,k} \delta t$$

on the radial boundary and so on. The boundary conditions given in section 2. 4. were derived to satisfy this requirement. The reason why barred velocity components $\bar{v}$ and $\bar{w}$ are used in the calculation of the intermediate internal energy $\tilde{I}$ also comes from this requirement. The total energy is not rigorously conserved when velocity components with or without tilde are used instead, although the analogue differential equations become the same as equations (3–5) to (3–8). Only the use of barred velocity conserves the total energy of the system.

The third term $\delta\tilde{E}^n_{cf}$ is expressed as follows

$$\delta\tilde{E}^n_{cf} = \delta t \delta r \delta\phi \sum_{jk} \frac{1}{2} \rho^n_{jk} w^n_{jk} (\tilde{v}^n_{jk} w^n_{jk} - v^n_{jk} \tilde{w}^n_{jk}), \tag{3–17}$$

and this term appears due to the presence of centrifugal force terms in the difference scheme in the polar coodinates. Because the difference between $\tilde{v}, \tilde{w}$ and $v, w$ is the order of $\delta t$, $\delta\tilde{E}^n_{cf}$ becomes the order of $(\delta t)^2$ and therefore it is higher than the rest of $\delta\tilde{E}^n_T$. It becomes negligibly small in practice if $\delta t$ is taken sufficiently small. $\delta\tilde{E}^n_{cf}$ disappears if $v$ is used instead of $\bar{v}$ in the calculation of intermediate internal enegy. For such scheme, however, energy defect appears and total energy is not conserved as mentioned before.

In Cartesian and cylindrical coordinates $\delta\tilde{E}^n_{cf}$ does not appear and similar discussion can be given to the rest. The total energy is rigorously conserved in these coordinates.

### *3.3.2. Mass and energy conservation in Phase II*

Mass flow $\delta M$ and total energy flow $E\delta M$ flowing out from any cell are regarded exactly as mass and total energy flows flowing into its adjacent cells respectively in Phase II. Therefore only the mass and energy flows across the boundaries of the computing region during the time increment $\delta t$ give the change of mass and total energy in the computing region. Since the boundary conditions are specified so as to represent the flows across the boundaries, the conservations of mass and total energy are satisfied in arbitrary coordinate system.

From above discussions it can be said that the FLIC difference schemes exactly conserve mass and total energy in Cartesian and cylindrical coordinates and also conserve them within the order of accuracy in the plane polar coordinates.

### *3.3.3. A modification in polar coordinates*

In the early stage of development of the PIC method, specific total energy $E$ was used as a primary variable in the energy equation. Internal energy was calculated by subtracting the kinetic energy from the total energy. Conservation of energy in the system, however, did not hold in this case and energy defect appeared although negligibly small in practice. In a certain kind of problem it brought an instability. Later the form in equation (1–4) was adopted and the trouble was relieved. In the PIC method it was necessary to assign the internal energy to each one of the particles, therefore the internal energy must be used explicitly as the one of the primary variables. In the FLIC method, however, there is no such requirement because of the reprresentation of the fluid as continuous medium. When the internal energy is used in Phase I, the centrifugal force terms are necessarily brought into the expression of $\delta\tilde{E}_T^n$, because the kinetic energy terms appear in $\delta\tilde{E}_T^n$ and the momentum equations must be substituted into them. When we adopt the specific total energy $E$ as a primary variable and use an energy equation expressed in terms of $E$ instead of the internal energy, the kinetic energy terms do not appear explicitly in the expression of $\delta\tilde{E}_T^n$ and the energy conservation is satisfied exactly in the polar coordinates.

A modification of the difference scheme is suggested as follows. Equation of energy (1–8) is replaced by

$$\rho\frac{\partial E}{\partial t}+\rho v\frac{\partial E}{\partial r}+\rho w\frac{\partial E}{r\partial\phi}+\frac{\partial[r(p+q)v]}{r\partial r}+\frac{\partial[(p+q)w]}{r\partial\phi}=0, \qquad (3\text{–}18)$$

and the intermediate total enery $\tilde{E}_{jk}^n$ is calculated by

$$\begin{aligned}\tilde{E}_{jk}^n=E_{jk}^n-\frac{\delta t}{\rho_{jk}^n V_j}\{&[S_{j+1/2}^r\bar{v}_{j+1/2,k}^n(p+q)_{j+1/2,k}^n-S_{j-1/2}^r\bar{v}_{j-1/2,k}^n(p+q)_{j-1/2,k}^n]\\&+S_k^\phi[\bar{w}_{j,k+1/2}^n(p+q)_{j,k+1/2}^n-\bar{w}_{j,k-1/2}^n(p+q)_{j,k-1/2}^n]\}.\end{aligned} \qquad (3\text{–}19)$$

The rest of the scheme remains unchanged from the one in section 2.2.

Total energy change $\delta\tilde{E}_T^n$ in Phase I now is expressed as

$$\begin{aligned}\delta\tilde{E}_T^n&=\sum_{jk}\rho_{jk}^n V_j(\tilde{E}_{jk}^n-E_{jk}^n)\\&=-\delta t\sum_k\{S_{j_m+1/2}^r\bar{v}_{j_m+1/2,k}^n(p+q)_{j_m+1/2,k}^n-S_{1/2}^r\bar{v}_{1/2,k}^n(p+q)_{1/2,k}^n\}\\&\quad-\delta t\sum_j S_k^\phi\{\bar{w}_{j,k_m+1/2}^n(p+q)_{j,k_m+1/2}^n-\bar{w}_{j,1/2}^n(p+q)_{j,1/2}^n\}.\end{aligned} \qquad (3\text{–}20)$$

It is clear that the energy is conserved exactly in this modified scheme. It can be shown that the consistency condition is also satisfied. In the present paper, however, the difference scheme given in section 2.2. were used because it was confirmed that $\delta E_{cf}^n$ was negligibly small without modification. Any comparison between the two schemes was not made.

## 4. Application to the Aerodynamic Problems

### *4.1. Supersonic flow past blunt bodies*

Supersonic flow past blunt bodies with detached shock waves has been investigated both theoretically and experimentally by various aerodynamicists, because the development of highspeed aircraft, launching vehicles and reentry vehicles needed the details of such flow field. As mentioned in the introduction, the flow field contains a discontinuous shock wave and the shock layer is divided into the regions where different type of a system of partial differential equations governs. Theoretical study may be classified roughly into three groups: analytical, numerical and computer experiment methods. Van Dyke [*36*] reviewed the existing analytical methods and showed that they are inadequate to find the details of flow near the blunt nose. He developed a numerical method of inverse type called "Marching-ahead Procedure". In his method, a curvelinear coordinate system is chosen to contain the shock wave as one of its surfaces and the basic equations are transformed into the coordinate system. They are solved numerically by forward integration from the shock wave toward the body surface as an initial value problem. The calculation must be repeated modifying the form of assumed shock wave until the desired body shape is obtained. Several modified versions are proposed by Vaglio-Laurin and Ferri [*37*], Fuller [*38*] and Lomax and Inouye [*39*]. Swigart [*40*] extended the method to the three-dimensional flow problem with an angle of attack. However, the inherent weak point of such inverse method lies on the fact that the calculated body shape is too sensitive to the change of assumed shock shape while the shock shape does not change significantly even by a large change of body shape in the real flow. So it is too hard to calculate a flow field past a body with sharp corner and of unusual form. On the other hand, the body shape is given as the previously known boundary condition in the direct numerical methods. But the difficulty as the mixed type nonlinear problem is not relieved. Hamaker [*41*] calculated flow past a circular cylinder at Mach number of infinity applying the relaxation method to the subsonic region and the method of characteristics to the supersonic region, respectively. He treated the sonic line separately where both of these methods are not applicable. He writes that the treatment of the sonic line is the most critical and difficult part of the entire calculation. Method of flux analysis by Uchida and Yasuhara [*42*] is a graphical method and not suitable for computer processing. Belotserkovskii, et al. [*43*] applied the method of integral relations to the blunt body problem. They made extensive calculations on inviscid, equilibrium and nonequilibrium flow fields around families of axisymmetric bodies. In this method, the boundary value problem is solved for an approximate system of ordinary differential equations using a polynomial approximation for the flow variables across the shock layer, along it or in both directions. The method is applicable only to the subsonic region. The calculation of the flow in the vicinity of sharp corner must be treated separately and it is considerably complicated.

When a time-dependent finite-difference method is applied to this kind of prob-

lem, the various assumptions, ristrictions and complicated procedures in the previous numerical methods are greatly reduced. The body shape is given as a previously-known boundary condition and no special treatment is required at a sharp corner. At the present stage of development there are several disadvantages such as difficulty of treatment of body surface which does not coincide with the computing mesh, low spacewise accuracy, stability of computation and long computing time. Shock wave and both of subsonic and supersonic regions of the shock layer, however, are obtained at once. The unsteady flow field as well as the steady one can be obtained because the calculation proceeds along the time axis as an initial-boundary value problem. In fact, the steady solution is given as a time-asymptotic solution after long time has passed.

Before we made the calculation of blunt body flow, a propagation of plane shock wave was computed in the plane polar coordinates in order to get the knowledge of the scheme in that particular coordinates. Initially a plane shock wave of shock Mach number 2.81 was placed in the middle of the computing region ABCD ($r=1.0\sim1.5, \delta r=0.01, \phi=0\sim90°, \delta\phi=1°$)in Fig. 2. The air in front of the shock was at rest and values given by R-H relation were assigned to the cells behind the shock. The parameters of artificial viscosity were set as $AK=1.5$ and $B=0.3$. The ratio $\tau$ of time increment $\delta t$ to radial cell width $\delta r$ was varied from 0.2 to 1.0. When $\tau$ was less than about a half of $\tau_{CFL}$, where $\tau_{CFL}$ is the maximum time increment ratio given by C-F-L condition, the result showed that the calculated shock Mach number, density and pressure jumps did not differ over one per cent from the exact R-H relation. The shock front kept to be plane as it propagated and the shock transition width was about three times of cell width. The oscillation just behind the shock was damped within one to two wave lengths. It can be said that the accuracy and the other characteristics of the scheme are almost same as the one in Cartesian and cylindrical coordinates.

*4.1.1. Supersonic flow past a circular cylinder*

Supersonic flow past a two-dimensional circular cylinder was calculated in the polar coordinates with the following conditions.

Computing region: ABCD in Fig. 2 where $r=1\sim3$, $\delta r=0.02$, $\phi=0\sim90°$, $\delta\phi=2.0°$, and body radius $R_b=1$,

Boundary conditions: reflective boundary at symmetric plane DA and on the body surface AB,
free stream boundary at upstream boundary CD,
and continuative boundary at downstream boundary BC,

Initial condition: impulsive start with free stream Mach number $M_\infty=4$, pressure $p_\infty=1$, sound speed $c_\infty=1$ and specific heats ratio $\gamma=1.4$,

Artificial viscosity parameters: $AK=1.5$, and $B=0.3$,

Time increment ratio: $\tau=\delta t/\delta r=0.1$.

Hereafter, length and time are nondimensionalized by the body radius $R_b$ and free stream sound speed $c_\infty$ as

$$r^*=r/R_b \quad \text{and} \quad t^*=tc_\infty/R_b.$$

Time history of shock stand-off distance $\delta_s/R_b$ given as the point of maximum radial derivative of pressure and time history of stagnation pressure coefficient $C_{ps}$ are shown in Fig. 3. The experimental steady shock stand-off distance and the exact stagnation pressure coefficient given by R-H and isentropic relations are also indicated in the figure. The shock asymptotically reached its steady position and the computation was stopped at the time cycle number $n=1200$, i.e. $t^*=2.4$. Shock shape and contour plot of local Mach number at this time are plotted in Fig. 4 where the broken lines indicate the shock width. Also in the figure are the shock and sonic line given by Moretti [*44*]. In Fig. 5, pressure distribution along the body surface at time $t^*=2.4$ is compared with a numerical solution by Fuller [*38*] and numerical and experimental results by Belotserkovskii [*43*]. Fine solid line indicates the sonic point on the body surface given by the position of the critical pressure. Radial pressure distribution across the shock layer at various angular positions are shown in Fig. 6 and compared with Moretti's result.

The computation required about four hours on Hitachi HITAC 5020F.

*4.1.2. Supersonic flow past a flat-faced circular cylinder*

The axisymmetric cylindrical coordinates was used for the calculation of flow

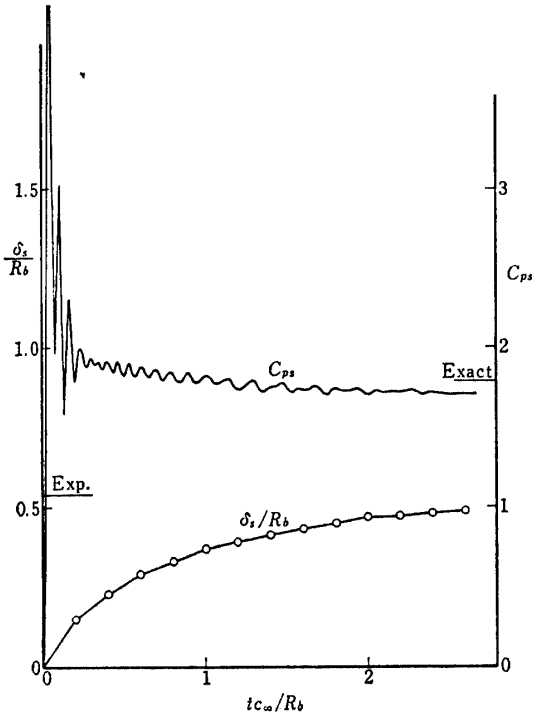


FIG. 3. Time history of shock stand-off distance and stagnation pressure coefficient of circular cylinder case, $M_\infty=4$.

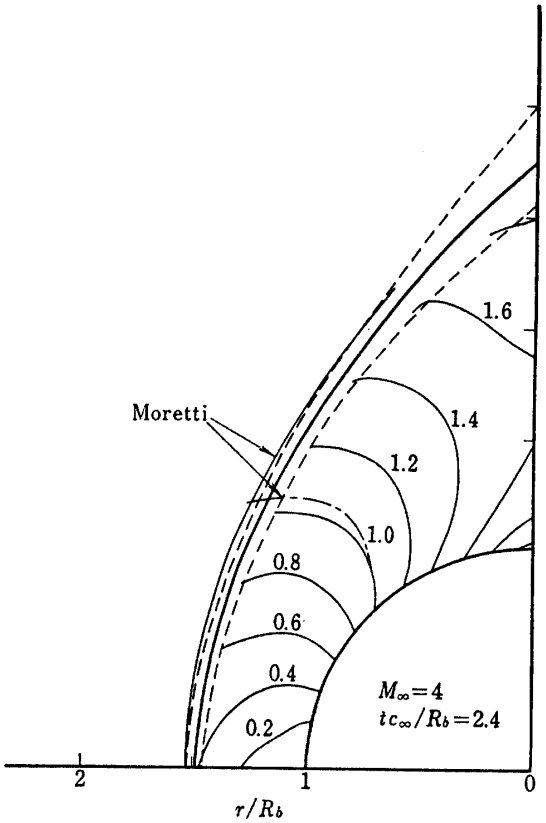


FIG. 4. Shock shape and contour plot of local Mach number around circular cylinder, $t^*=2.4$ and $M_\infty=4$.

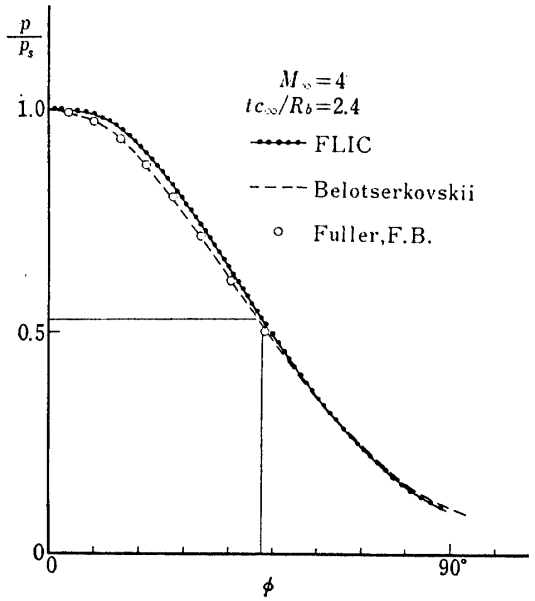


FIG. 5. Pressure distribution on the body surface of circular cylinder, $t^*=2.4$ and $M_\infty=4$.

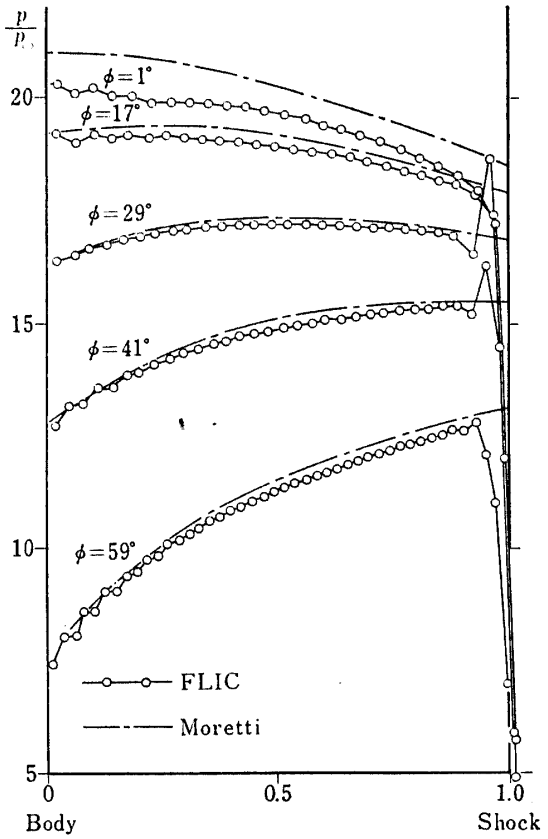


FIG. 6. Radial pressure distribution across the shock layer of circular cylinder at various angles, $t^*=2.4$ and $M_\infty=4$.

past a flat-faced circular cylinder. In Fig. 1, the computing region is expressed as follows

$$x/R_b=-2.0\sim+1.0,\ \delta x=1.0,\ r/R_b=0.0\sim2.5,\ \delta r=1.0,$$
and body radius $R_b=20\delta r$.

The initial and boundary conditions are the same as in the previous section except for the free stream Mach number $M_\infty=2.81$ and time increment ratio $\tau=\delta t/\delta x=0.2$. Shock stand-off distance and stagnation pressure coefficient are plotted against time and compared with the experimental result by Kendal [*45*] and the exact pressure coefficient respectively in Fig. 7. The change of the flow field becomes almost negligible after time $t^*=4$. As the asymptotic steady solution the flow field at $t^*=8$ is shown in Fig. 8. These contour maps were obtained using X-Y plotter directly from the output from the computer. Each plot is normalized by each free stream value except for the local Mach number which represents the absolute value. The interval between the contour lines is 0.1, 0.2, 0.5 and 0.2 for Mach number, density, pressure and internal energy, respectively. The bow shock wave in front of the body is expressed by many close contour lines. The irregular pattern found in the free stream region is due to the round-off errors in the computation of plot

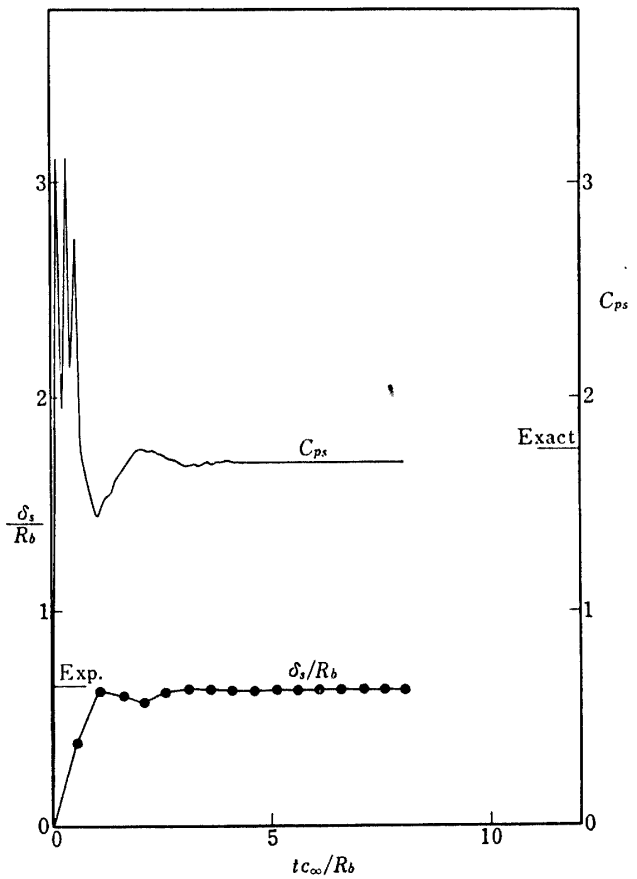


FIG. 7. Time history of shock stand-off distance and stagnation pressure coefficient of flat-faced cylinder case, $M_\infty=2.81$.

routines and it is meaningless as well as some of the symbols and digits in the plots such as M JET and T. In Fig. 8(e) the steady streamlines were computed based on the mass conservation law. The bow shock wave in the figure was determined by the least-square polynomial fitting to the trail of maximum axial pressure derivative points at each radius. Pressure distributon along the body surface normalized by the stagnation point pressure is compared with the numerical result by South [*46*] at the front side of the body and with the experimental one by Kendal at the afterbody side in Fig. 9.

### *4.2. Supersonic opposing jet directed upstream against supersonic main stream*

The flow field around blunt bodies in a supersonic main stream induced by a supersonic opposing jet injection from the nose is an area of interest. Opposing jet injection is considered as a means of aerodynamic heat alleviation at atmospheric reentry and flight control of highspeed aircraft and rockets. Most investigations of such a flow field have been made experimentally and the theoretical studies are quite few because of its highly complicated flow phenomena. Watt [*47*] investigated the interaction of sonic jet directed upstream against main stream of Mach number 2.5 by Schlieren photographs. Charczenko and Hennessey [*48*] found drag reduction and instability of flow field of Apollo Command Module

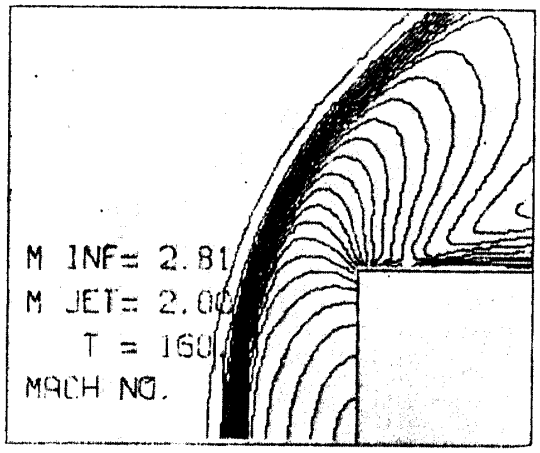


FIG. 8. (a) local Mach number.

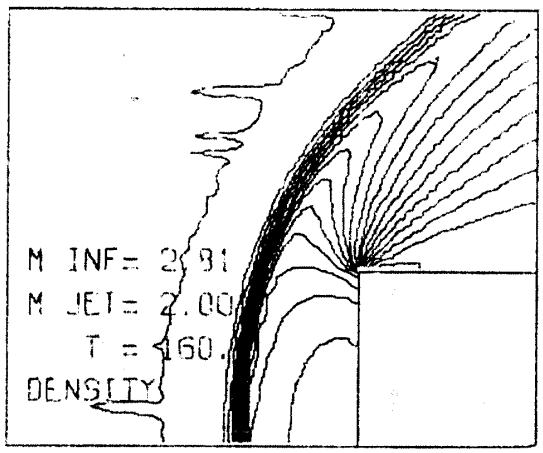


FIG. 8. Continued, (b) density.

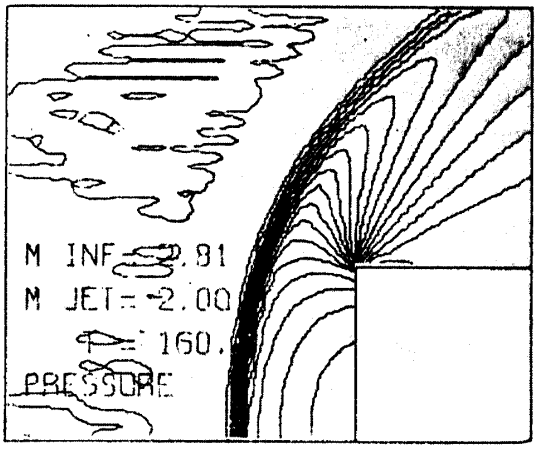


FIG. 8. Continued, (c) pressure.

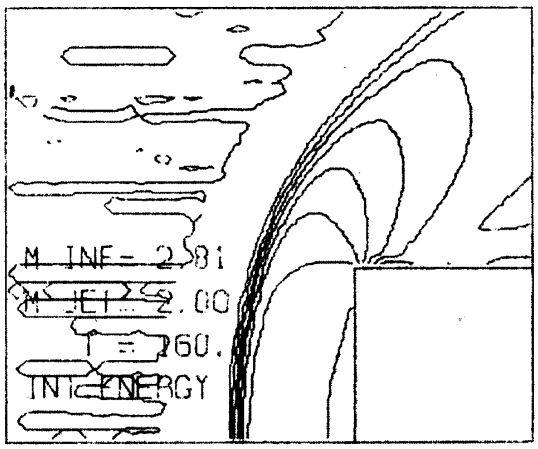


FIG. 8. Continued, (d) internal energy.

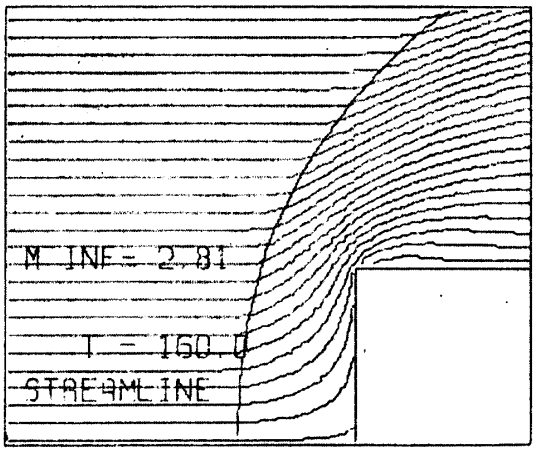


FIG. 8. Concluded, (e) streamlines and bow shock wave.

FIG. 8. The asymptotic steady flow field around flat-faced cylinder as given by countour plots, $t^*=8$ and $M_\infty=2.81$.

model with retro jet injection. Hayman and McDearmon [*49*] investigated the effects of total pressure ratio of the jet to the free stream, jet-exit Mach number and nozzle to body radius ratio on the flow pattern using flat-faced circular cylinder model in Mach 2.91 main stream. Romeo and Sterrett [*50*] made similar experiment at main stream Mach number of 6. They found two different types of the

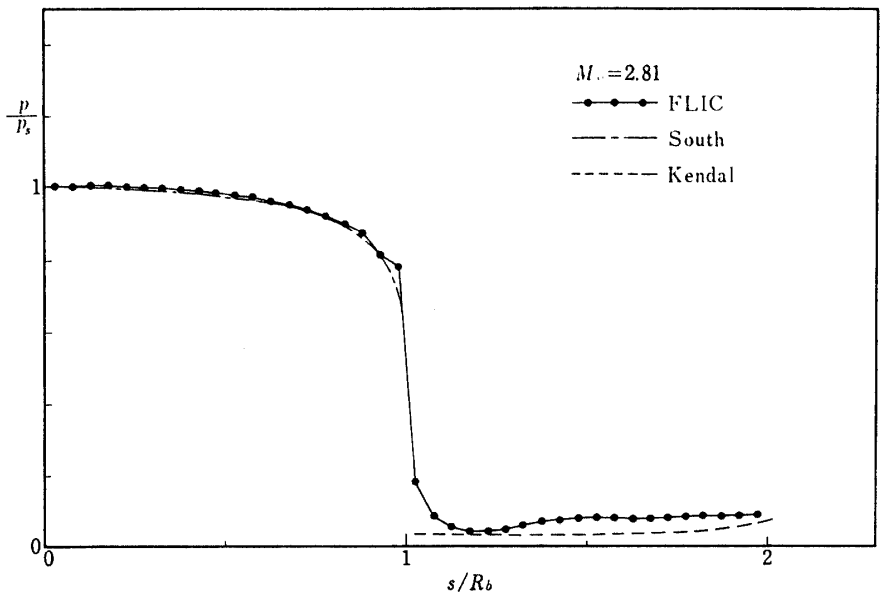


FIG. 9. Pressure distribution on the body surface of flat-faced cylinder, $t^*=8$ and $M_\infty=2.81$.

field. At high total pressure ratio, Mach disc is formed in the jet exhaust and stationary bow shock wave similar to the one in front of a blunt body in a supersonic flow is observed in the main stream. The structure of the jet is qualitatively the same as the one of the underexpanded jet flow into still air. Another type occurs at low total pressure ratio and is characterized by unsteady behaviour of the jet with violent oscillation of the bow shock in the main flow direction and the Mach disc is not formed inside the jet stream. They attribute the latter type to the predominant viscous dissipation of jet mixing along the jet stream boundary. They explained the both types of the flow field by a simple qualitative theoretical analysis. Casanova and Wu [*51*] gave a semi-empirical formula for the stand-off distance of the bow shock. However, in the treatment of the problem, it seems that the analytical and ordinary numerical approaches are difficult even for the steady type, because the flow field contains more than two shock waves, the interface between the main and the jet streams and both of subsonic and supersonic regions. It is more complicated than a simple blunt body problem. The time-dependent finite-difference method will be applicable to the calculation of such entire flow field if the calculation is carefully made.

In the present study the flow field induced by a supersonic opposing jet from the nose of a flat-faced circular cylinder is investigated applying the FLIC method. The calculation was restricted within the supersonic opposing jet because no disturbance in the flow field may not propagate upto and change the flow inside the jet nozzle and the boundary condition can be strictly given at the nozzle exit. It will not be so in the case of subsonic jet injection although Taylor and Masson [*52*] calculated such case applying Godunov's scheme.

The concept of the problem and cell arrangement are depicted again in Fig. 1. The axisymmetric cylindrical coordinates are used as in the case in the previous

TABLE 1. Aerodynamic parameters and initial conditions for the opposing jet problem.

| Case No. | $M_\infty$ | $M_j$ | $p_{0j}/p_{0\infty}$ | $I_j/I_\infty$ | $R_j/R_b$ | $(tc_\infty/R_b)_{\text{last}}$ | Initial Condition |
|---|---|---|---|---|---|---|---|
| A | 2.81 | 2.81 | 5 | 1 | 0.5 | 10 | Steady flow around flat-faced cylinder for $M_\infty=2.81$ |
| B | 2.81 | 2.81 | 5 | 1 | 0.5 | 5 | Same as Case A |
| C | 3.00 | 3.00 | 2 | 1 | 0.25 | 12 | Impulsive start with impulsive jet injection |
| D | 2.81 | 2.81 | 2 | 1 | 0.5 | 10 | Same as Case A |

section. The body is represented by the rigid boundary cells where the reflective condition is applied as the boundary condition for the difference scheme. Boundary condition at the jet nozzle exit is given by the jet nozzle cells where the values of the flow variables are set to be equal to those of the opposing jet exit condition. At the outer boundaries of the computing region, similar conditions as in the previous section are given and shown in the figure.

Four different cases were calculated in the present study. The aerodynamic parameters and the initial conditions for each case are listed in Table 1 where $M_\infty$ and $M_j$ are the free stream and jet exit Mach numbers respectively, $p_{0j}/p_{0\infty}$ and $I_j/I_\infty$ are the total pressure and internal energy ratios of the jet to the free stream respectively, and $R_j/R_b$ is the nozzle to body radius ratio. The time $(tc_\infty/R_b)_{\text{last}}$ means that the calculations was produced up to this time. Pressure $p_\infty$ and sound speed $c_\infty$ of the free stream are normalized to unity. The free stream gas and the jet gas are the same kind with specific heats ratio $\gamma=1.4$. The steady flow field obtained in the previous section was used as the initial condition

TABLE 2. Parameters for the finite-difference calculations.

| Case No. | *IN*1 | *IN*2 | *JETIN* | *JN*1 | *JN*2 | *JETJN* | AK B | $\frac{\delta x}{\delta r}$ | $\frac{\delta t}{\delta x}$ | Computing Region |
|---|---|---|---|---|---|---|---|---|---|---|
| A | 100 | 20 | 0 | 20 | 30 | 10 | 1.5<br>0.3 | 1.0<br>1.0 | 0.2 | $x/R_b=-5\sim+1$<br>$r/R_b=0\sim2.5$ |
| B | 40 | 40 | 0 | 10 | 40 | 5 | 1.5<br>0.3 | 2.0<br>2.0 | 0.2 | $x/R_b=-4\sim+4$<br>$r/R_b=0\sim5.0$ |
| C* | 100<br>(135) | 20 | 0 | 20 | 30<br>(20) | 5 | 1.5<br>0.3 | 1.0<br>1.0 | 0.2 | $x/R_b=-5\sim+1$<br>$r/R_b=0\sim2.5$ |
| D | 100 | 20 | 0 | 20 | 30 | 10 | 1.5<br>0.3 | 1.0<br>1.0 | 0.2 | $x/R_b=-5\sim+1$<br>$r/R_b=0\sim2.5$ |

* ( ), after $t^*=9$

for all but case C in which the free stream values were allotted to every cell at the start of computation. We regarded the opposing jet was already started at time zero. Jet flow deflection angle at the nozzle exit was set to be zero, although the other conditions can be easily applied if one wishes so. The other parameters for the difference scheme are shown in Table 2. Symbols such as IN1, IN2 and JETIN represent the total cell numbers taken in axial and radial directions as shown in Fig. 1. Time increment ratio $\tau$ was 0.2 in all cases. Case B was cal-

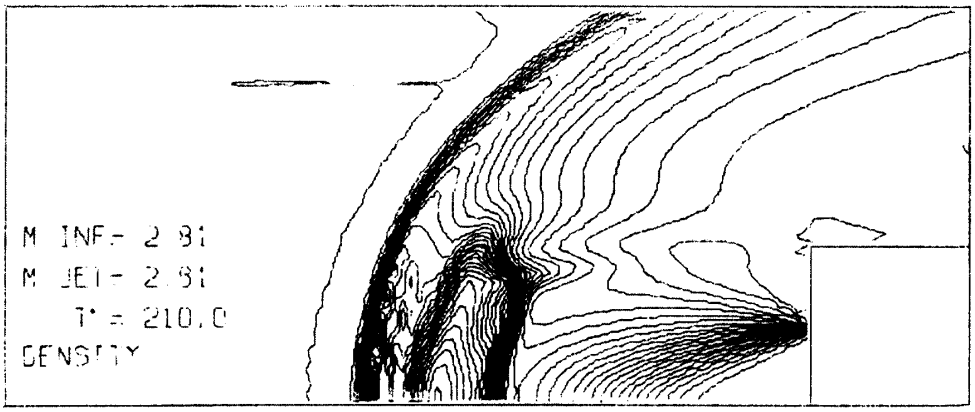


FIG. 10. (a) $t^*=2.5$.

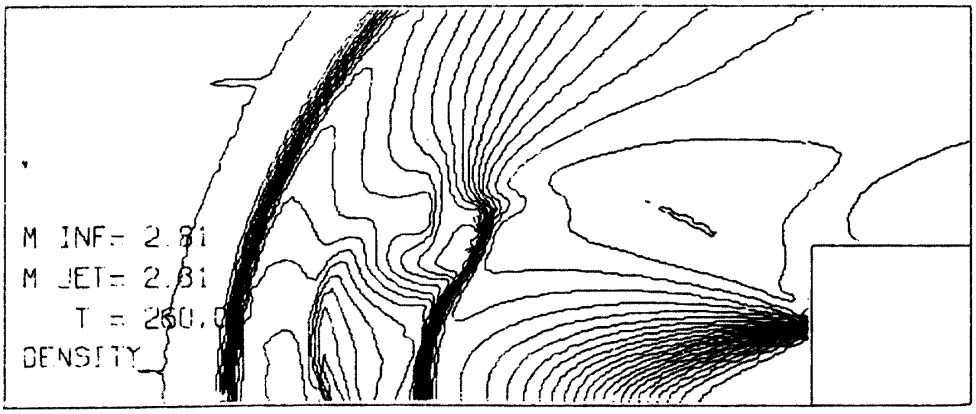


FIG. 10. Continued, (b) $t^*=5.0$.

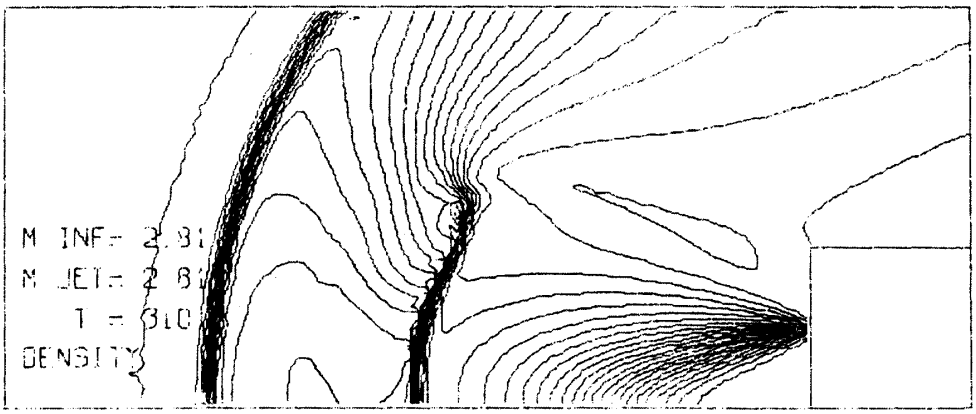


FIG. 10. Continued, (c) $t^*=7.5$.

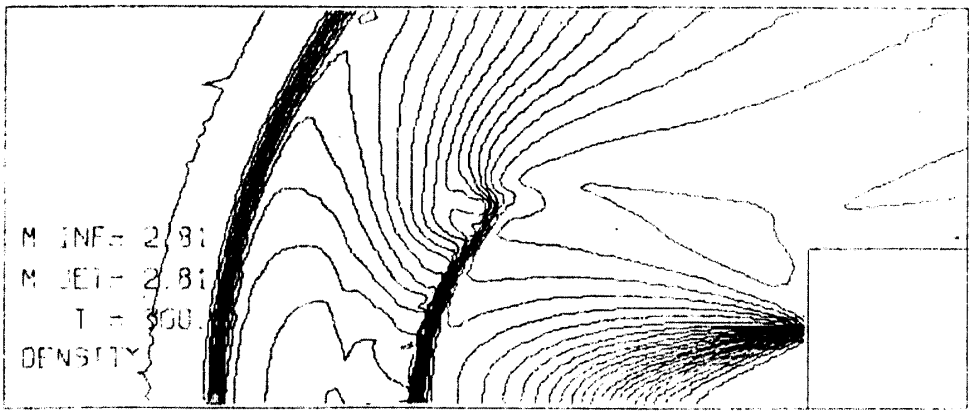


FIG. 10. Concluded, (d) $t^*=10.0$.

FIG. 10. Time-dependent flow field of the opposing jet as given by countour plots of density, case A.

culated to check the influence of the boundary conditions and the accuracy of solution. Aerodynamic parameters were identical with case A and cell size was doubled to enlarge the computing region.

The following figures are the examples of the computer plots of the results of the calculation. Fig. 10 shows the isopicnic lines at nondimensionalized time $t^*=tc_\infty/R_b)=2.5$, 5.0, 7.5 and 10.0 of case A. The total pressure ratio is five. The

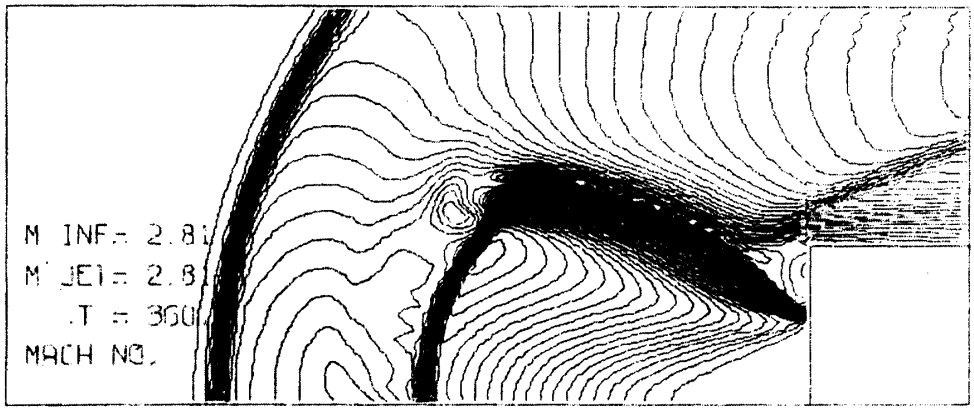


FIG. 11. (a) local Mach number.

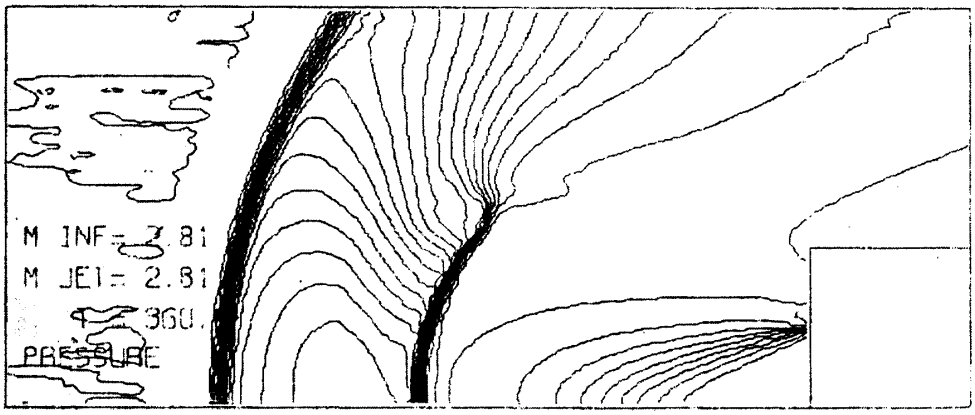


FIG. 11. Continued, (b) pressure.

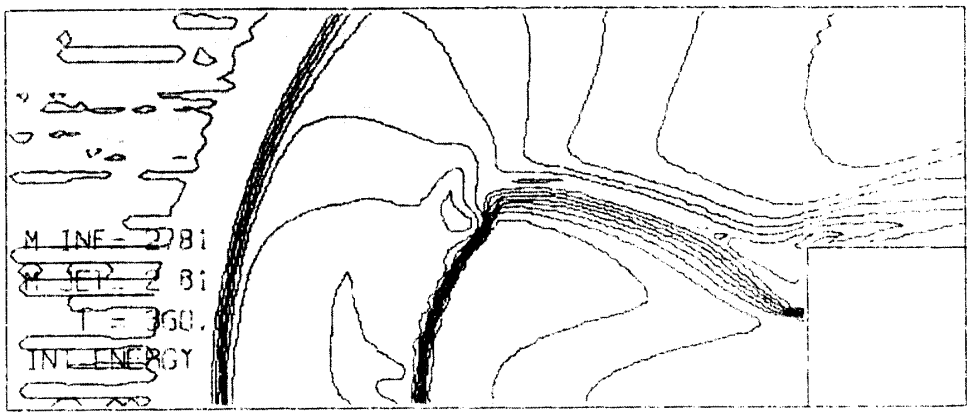


FIG. 11. Continued, (c) internal energy.

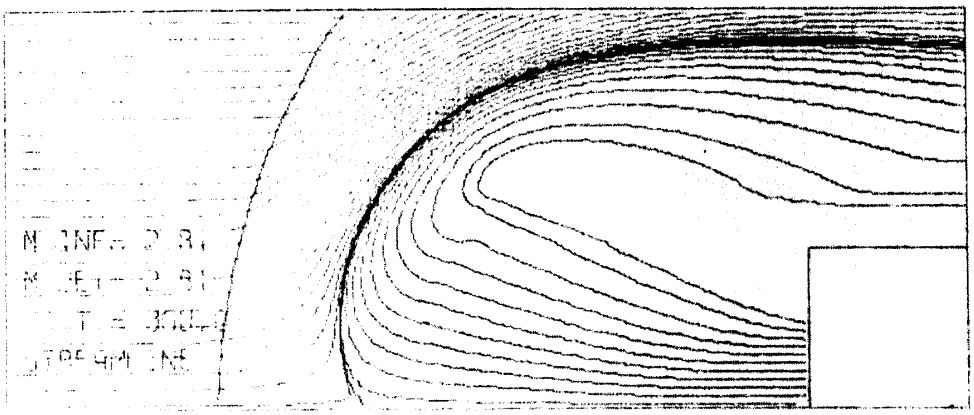

FIG. 11. Continued, (d) Streamlines and bow shock wave.

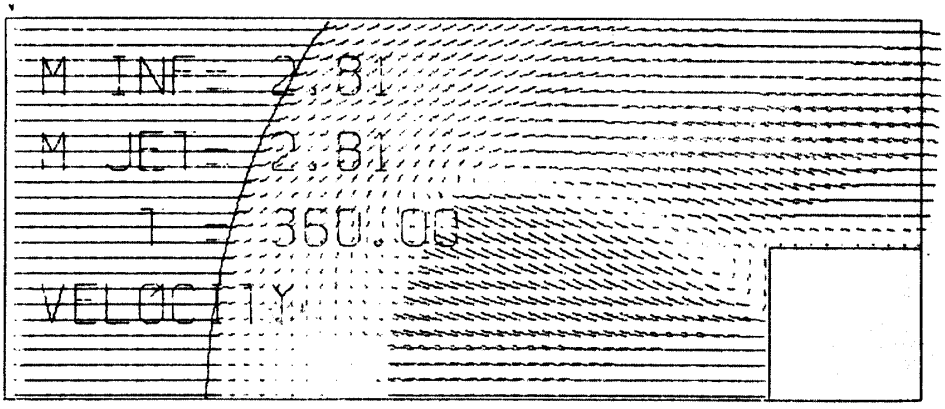


FIG. 11. Concluded, (e) velocity vectors.

FIG. 11. The asymptotic steady flow field of case A at $t^*=10$.

rectangular frame in the figure indicates the entire computing region. The lower boundary is the symmetric axis and the flat-faced cylinder lies on the lower right corner. "T" in the figures does not indicate the correct time and should be neglected because it means the value of $n\delta t$ continuing from the calculation in the previous section. The intervals between the contour lines are the same as in Fig. 8 except case C in which the intervals are 0.1 for density, local Mach number

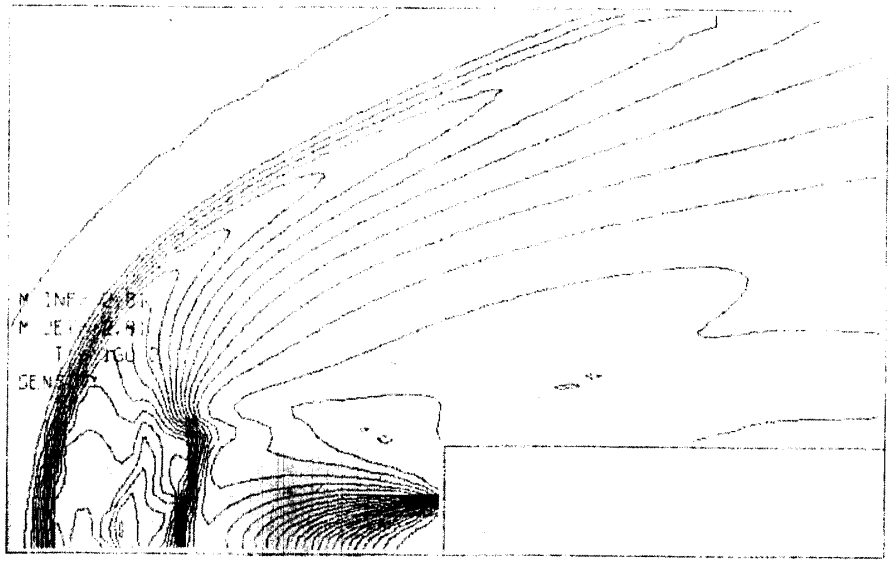

FIG. 12. Isopicnic lines of case $B$, $t^*=5$.

and internal energy and 0.2 for pressure, respectively (see Figs. 13 and 14). The contour maps of local Mach number, pressure, and internal energy, stream lines and velocity vector at every other cell at time $t^*=10$ are shown in Fig. 11 as the asymptotic steady flow field. To compare with case A, the isopicnic lines at time

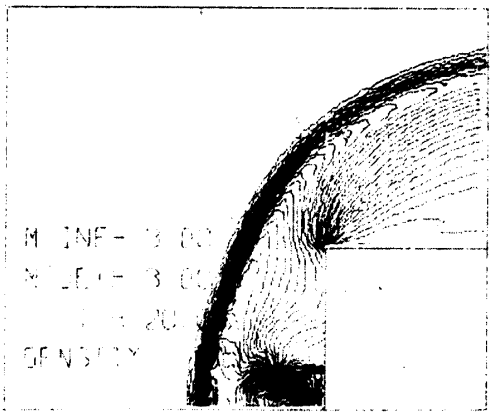

FIG. 13. (a) $t^*=1$.

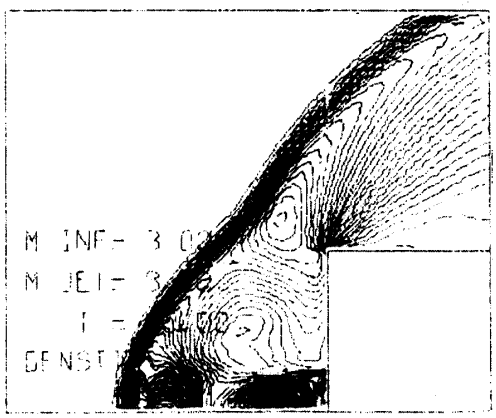

FIG. 13. Continued, (b) $t^*=2$.

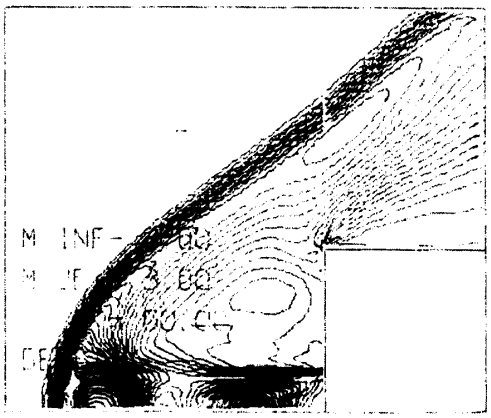

FIG. 13. Continued, (c) $t^*=3$.

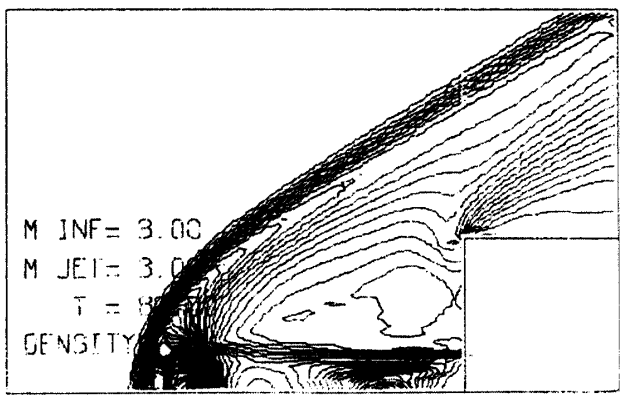


FIG. 13. Continued, (d) $t^*=4$.

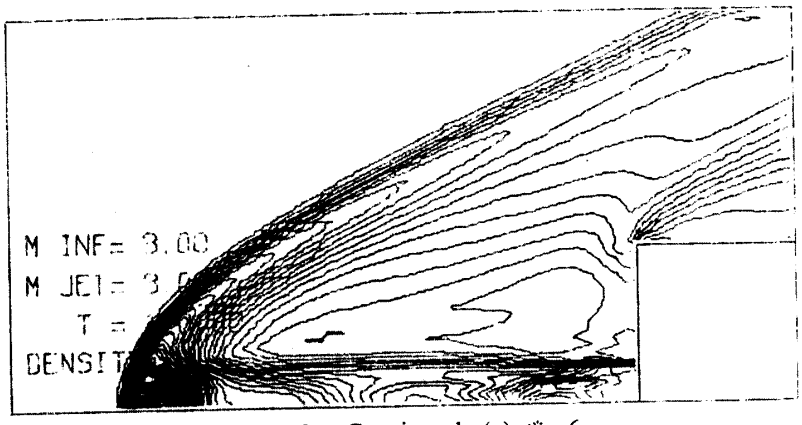


FIG. 13. Continued, (e) $t^*=6$.

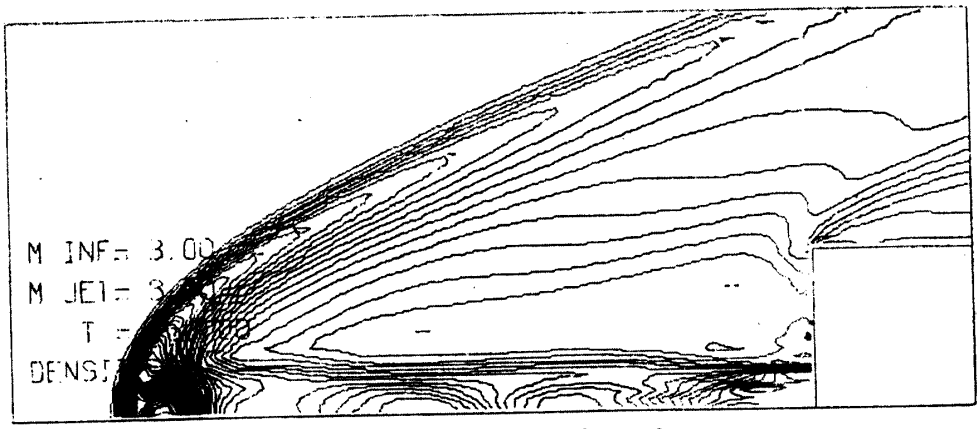


FIG. 13. Continued, (f) $t^*=8$.

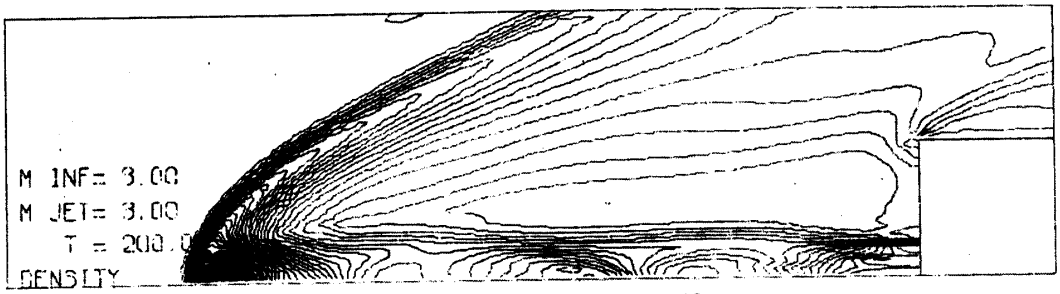


FIG. 13. Continued, (g) $t^*=10$.

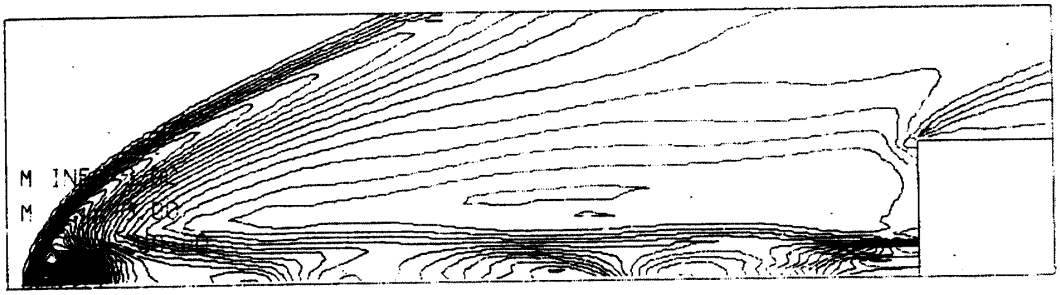

FIG. 13. Concluded, (h) $t^*=12$.

FIG. 13. Time-dependent flow field of the opposing jet as given by a series of contour plots of density, case C.

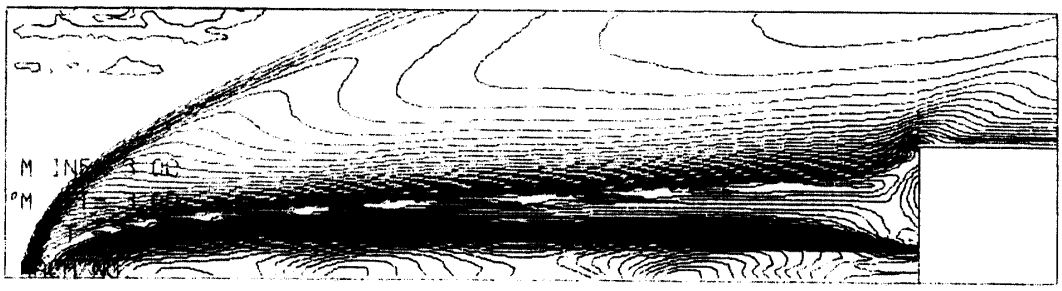

FIG. 14. (a) local Mach number.

FIG. 14. Continued, (b) pressure.

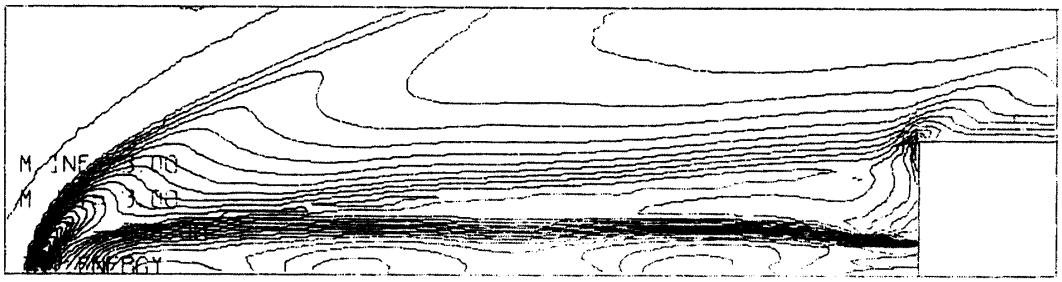

FIG. 14. Concluded, (c) internal energy.

FIG. 14. Unsteady flow field of case C at $t^*=12$.

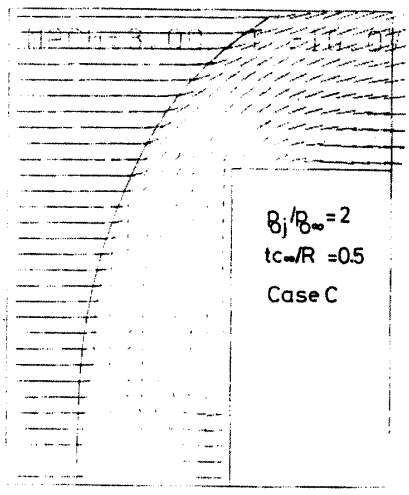


FIG. 15. (a) $t^*=0.5$.

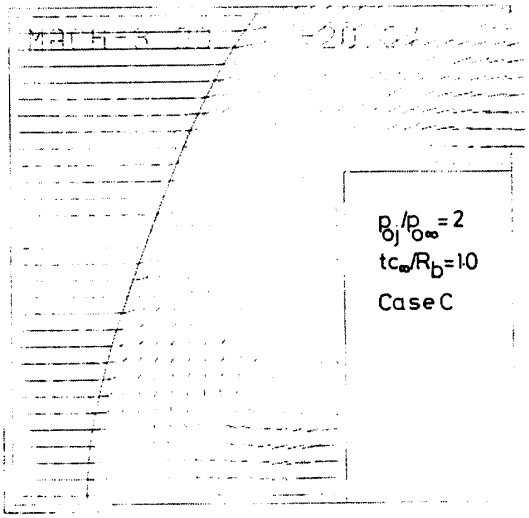


FIG. 15. Continued, (b) $t^*=1.0$.

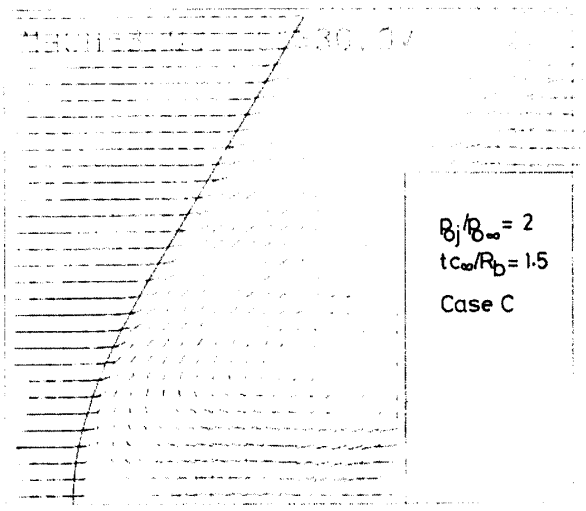


FIG. 15. Continued, (c) $t^*=1.5$.

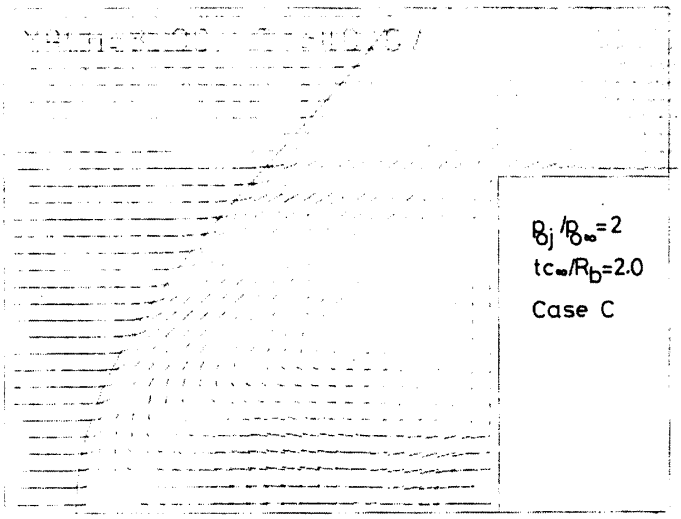


FIG. 15. Continued, (d) $t^*=2.0$.

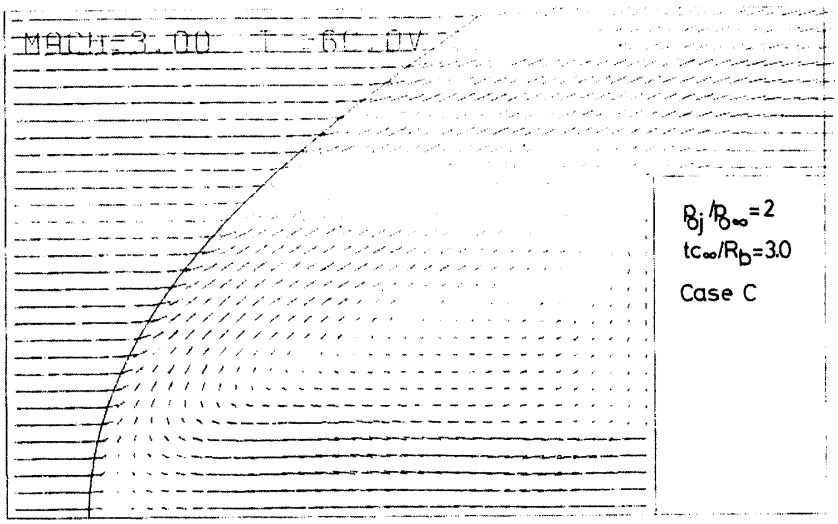


FIG. 15. Continued, (e) $t^*=3.0$.

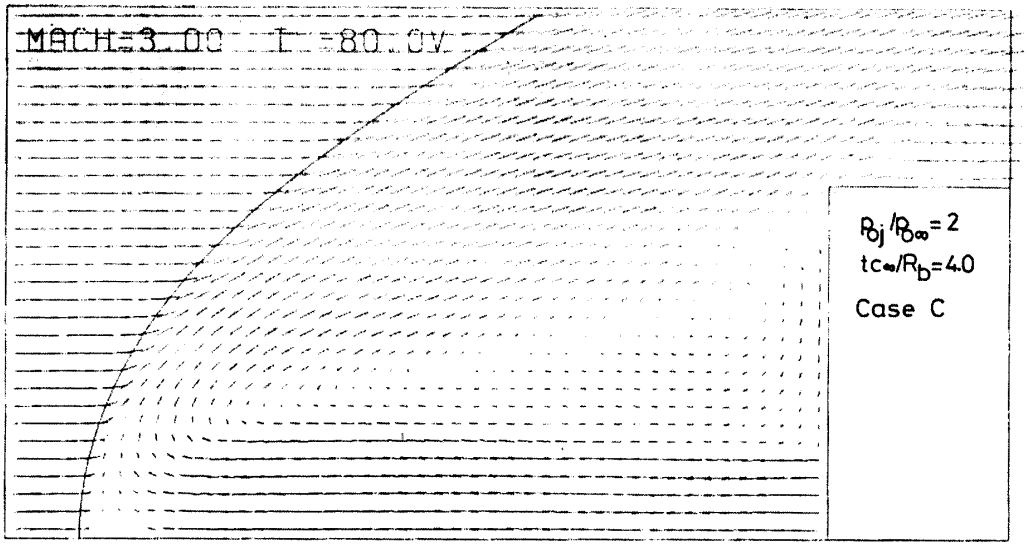


FIG. 15. Concluded, (f) $t^*=4.0$.

FIG. 15. Details of flow field in the vicinity of nose in the early stage of case C as given by velocity vectors.

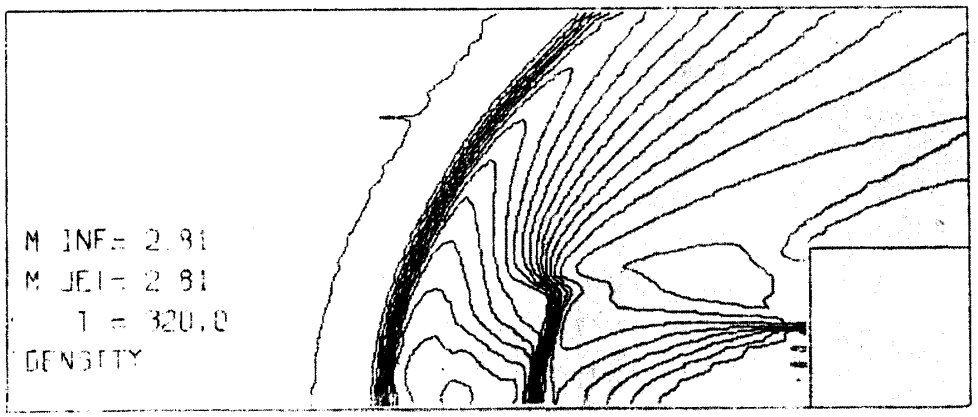


FIG. 16. (a) density.

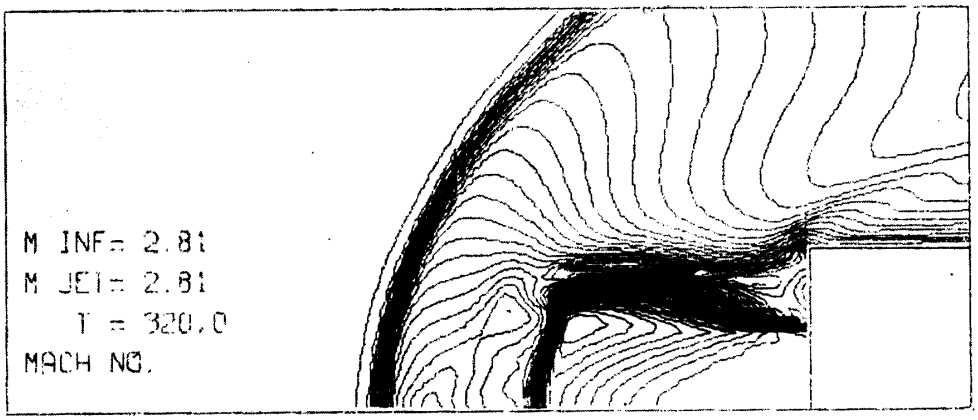


FIG. 16. Continued, (b) local Mach number.

$t^*=5$ of case B are shown in Fig. 12. The time-dependent flow field of case C is shown in Fig. 13 as a series of isopicnic line plots. The total pressure ratio is two and the nozzle exit radius is one fourth of the body radius. The free stream and the jet were impulsively started in this case. The bow shock was formed soon after the start and moved forward as the core of the jet stream extended along the axis. When the bow shock reached near the upstream boundary at time $t^*=9$, the computing region was extended forward and shortened in radial direc-

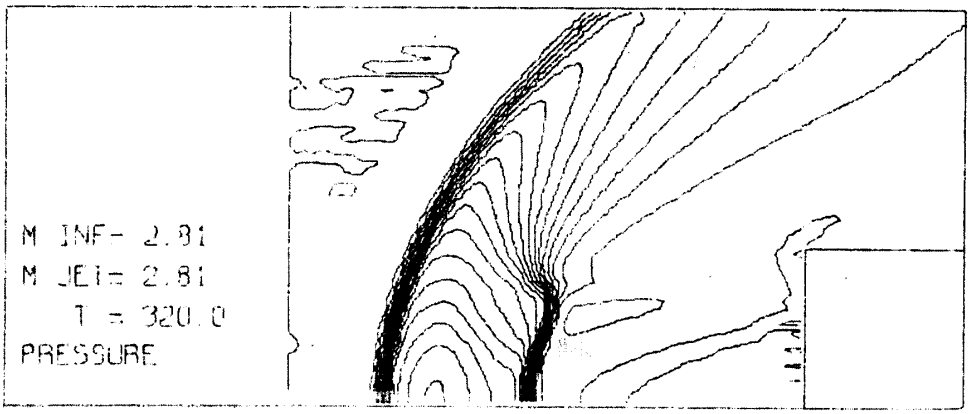


FIG. 16. Continued, (c) pressure.

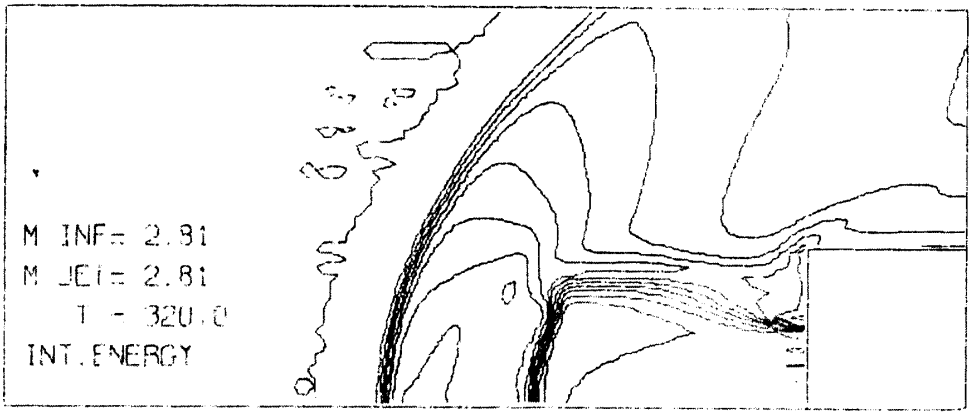


FIG. 16. Continued, (d) internal energy.

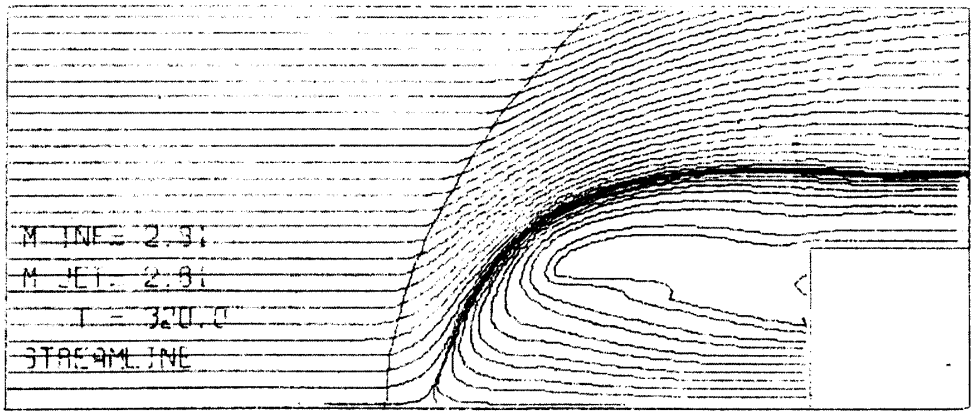


FIG. 16. Continued, (e) streamlines and bow shock wave.

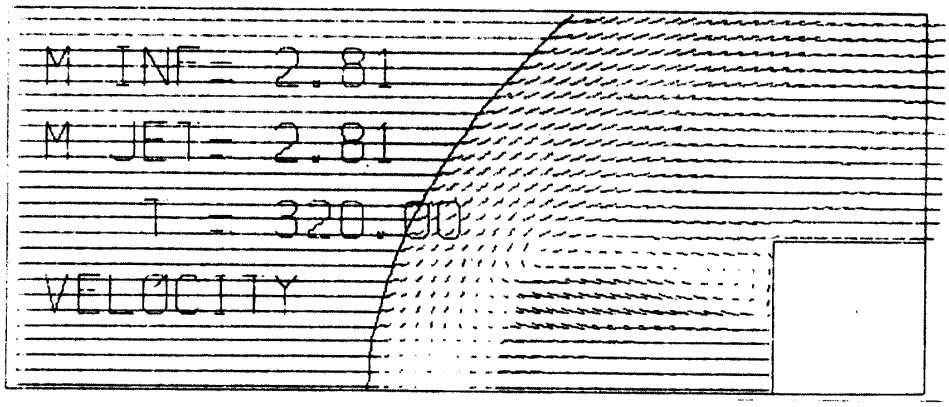


FIG. 16. Concluded, (f) velocity vectors.

FIG. 16. The asymptotic steady flow field of case D at $t^*=10$.

tion. The computation was continued until time $t^*=12$ when the shock again reached the upstream boundary. Fig. 14 shows the unsteady flow field at time $t^*=12$. The details of the flow field in the vicinity of the nose at early time are shown in Fig. 15 where the velocity vector at every cell is plotted. The solid line indicates the bow shock. The steady flow field was obtained for case D in which the total pressure ratio was two and the other conditions were identical with case A. Flow field at time $t^*=10$ is shown in Fig. 16.

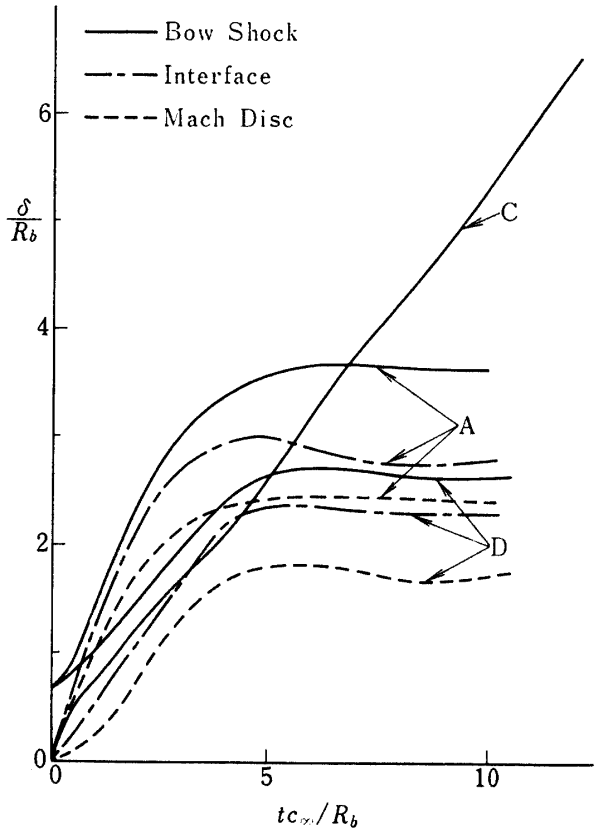


FIG. 17. Time history of stand-off distances of bow shock, interface and Mach disc.

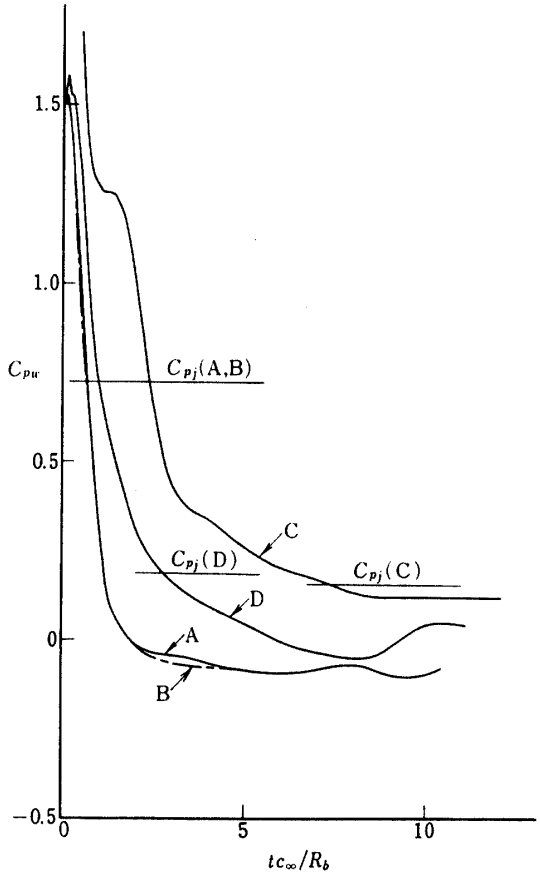


FIG. 18. Time history of average surface pressure coefficient.

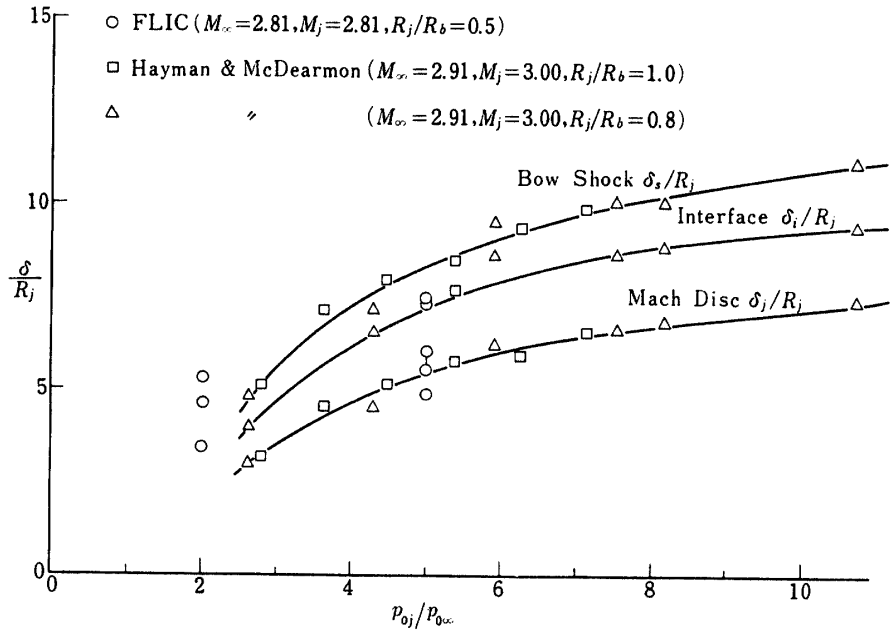


FIG. 19. Variation of stand-off distances with total pressure ratio.

The stand-off distances of the bow shock, the interface and the Mach disc are plotted against time in Fig. 17. Fig. 18 shows the time history of the average surface pressure coefficient on the front side except the nozzle area. Jet exit static pressure for each case is also indicated by horizontal line. Experiments of Hayman and McDearmon were made with aerodynamic conditions close to the ones in the present study, i.e. main stream Mach number $M_\infty=2.91$, jet exit Mach number $M_j=3.00$ and nozzle to body radius ratio $R_j/R_b=0.8$ and 1.0. Standoff distances read from their experimental photographs were plotted as function of total pressure ratio in Fig. 19 and compared with the present results of case A and D indicated by white circles. In this figure the stand-off distances were normalized by the jet nozzle radius $R_j$.

The computation required about 4 millisecond per one time cycle and one cell using the same computer as in the previous section. The whole calculation took about six hours for each of cases A and C, one hour for case B and three and a half hour for case D. In the last case the most of the free stream region in front of the bow shock was left without computation at each time cycle to save the computing time.

## 5. Discussions of the Results

### *5.1. Supersonic flow past blunt bodies*

#### *5.1.1. Asymptotic behaviour to the steady flow field*

A bow shock wave is formed upon the body surface when the body impulsively begins to move. In the two-dimensional circular cylinder case, the shock wave moves forward with decreasing speed and approaches monotonically its final position. But the final steady state was not attained within the computing time $t^*=2.4$. The shock stand-off distance was approximately expressed as an exponential function of time and the extrapolated steady value was $0.52\ R_b$. The moving shock wave was attenuated from the start by diffraction waves originating from every point on the body surface. The stagnation pressure showed an oscillation with small amplitude, the period of which proportionally increased with the shock stand-off distance. The period was characterized by a representative time $\tau_\delta(=\delta_s/c_s\cdot c_\infty/R_b\leq 0.257)$ where $c_s$ is the sound speed behind the shock. This indicates that the oscillation results from the pressure wave propagation between the shock and the body surface. The pressure approaches steady state faster than the shock stand-off distance does.

On the other hand, in the flat-faced cylinder case, the shock wave left the front surface with nearly constant speed and overshot beyond the steady position then approached the equilibrium position accompanying slow and large oscillation. The stagnation pressure varied with phase opposite to the oscillation of shock stand-off distance, i.e. pressure decreased as the shock moved forward and increased as the shock moved backward. The period of the pressure oscillation coincided with the twice of a representative time $\tau_r(=R_b/c_s\cdot c_\infty/R_b=0.62)$ which means the time

the presence of the corner reaches the center line. Such oscillation of shock is in contrast with the former case. Miles, Mirels and Wang [*53*] gave a theoretical required time for establishing the detached shock around an impulsively started flat-faced cylinder. Their theory gives time $t^*=2.92$ for free stream Mach number of 2.81 which agrees with the present result. However, their assumption that the shock monotonically reaches the steady position seems to be a crude one when we consider the oscillating behaviour of the shock found in the present calculation.

*5.1.2. Steady flow field*

The steady shock stand-off distance around a circular cylinder parallel to the main stream agreed with the experimental results by Kim [*54*] and Ambrosio and Wortman [*55*] and with the existing numerical results. A little difference of the shock wave position at time $t^*=2.4$ from Moretti's calculation was due to the remaining unsteadiness. But the shock shape itself was in good agreement and seems to coincide with his result after a long time because it still keeps moving forward slowly. Therefore the flow just behind the shock did not become steady perfectly at this time while the flow near the body surface had already approached steady state as indicated by the coincidence of the shape of the sonic line in both results in Fig. 4. The sonic point on the surface was at $\phi=47.5°$. In spite of the coarse cell arrangement in angular direction, the present calculation showed a close agreement with other numerical and experimental results.

The contour plot of local Mach number qualitatively showed similar pattern to Hamaker's solution for infinite Mach number. Some distortion was recognized in the region near the down stream boundary where the continuative boundary condition was applied. However, the influence of the boundary condition did not propagate deep into the upstream because the flow was purely supersonic there. Distribution of the surface pressure also showed a favorable curve close to the other existing results. The value of stagnation pressure $p_s/p_\infty$ was 20.29 which was about 3 per cent lower than the exact one 21.075.

In the flat-faced cylinder case, the shock stand-off distance $\delta_s/R_b$ (=0.632), and the shapes of the shock and the sonic line were in better agreement with experiments than in the former case. Contour plots indicate that the sonic line leaves exactly from the body shoulder and surface pressure decreases to lower than the critical pressure there. Surface pressure agreed with South's numerical solution by the method of integral relations. The comparison of the shock shape between the present and his results indicates that the former gives reasonable shock shape and flow field around the body shoulder and the latter does significantly different shock shape from the experimental one. The region of low local Mach number extends to the vicinity of the shoulder compared with the one past a circular cylinder. Therefore the shape of the corner will have a large effect on the flow pattern of the entire shock layer. A weak secondary shock is formed behind the expansion around the shoulder. Compared with experiments, the pressure distribution on the side surface indicates the shock originates from nearer position to the shoulder than experiments. It may be caused by the insufficient

body length used in the presnt calculation and neglected real viscosity effect which may play main role on the separation and reattachment of the flow past the shoulder.

### *5.1.3. On some numerical problems in the polar FLIC method*

A large oscillation with wave length of 2 to 3 $\delta r$ occurred in the region $\phi=40°\sim50°$ in the early stage of computation in the polar coordinates. This oscillation seems to arise from the nonlinear instability of the difference scheme because the region includes the sonic line inside where the instability tends to occur as well as at the stagnation point. However, it was damped down subsequently by the dissipative effect of the truncation error terms and the solution converged to a smooth one after all. Moretti [*56*] pointed out that the reflective boundary condition represents zero radial derviative on the body surface and it is physically incorrect in general. He showed that correct pressure distribution across the shock layer was not obtained and sometimes the solution became unstable when the reflective boundary condition was applied. Applying time-dependent method of characteristics to the calculation on the body surface and at the shock front, he obtained a smooth pressure distribution across the shock layer using only a few mesh points across it. Comparing with his results in Fig. 6, a reasonable distribution is obtained when a fine mesh is used in the FLIC method even if the reflective boundary condition is applied. In the figure, the largest deviation of a few per cent occurred on the stagnation stream line $\phi=0°$. This error was caused by the accuracy of the method, cell size and cell arrangement, i.e. the stagnation streamline is not located on the center of cell. The magnitude of the error, however, remained within the same order as that of two-dimensional problems in other coordinates.

Oscillation of shortest wave length $2\,\delta r$ is most hard to decay because the amplification matrix becomes unity for such wave length as pointed out by Houghton, Kasahara and Washington [*57*] who discussed the stability of Lax-Wendroff scheme. The present calculation exhibits the same tendency as in their case. Such shortest wave remained to the last in the vicinity of body surface. But the oscillation became sufficiently small after all. Another oscillation just behind the shock jump is unavoidable due to the continuous transition across the shock in the present method.

Conservation of total energy in the computing region was checked throughout the computation and it was confirmed that the net change of total energy during the time increment $\delta t$ was less than $10^{-3}$ of the total energy $E_T^n$ in the computing region. Therefore the total energy is conserved practically in the polar coordinates as well as in the other coordinates.

### *5.2. Supersonic opposing jet directed upstream against supersonic main stream*

The results of the calculation indicate that there are two different types of flow field. One of them is a steady flow field which was obtained asymptotically as time tends to infinity. Such as example is case A. The other type is obtained

for case C in which the flow field consists of ever-forward-moving bow shock and periodic wave pattern inside the jet stream. The discussions are given as follows.

*5.2.1. Asymptotic behaviour to the steady flow field*

To establish the supersonic opposing jet flow, the normal shock wave formed in the nozzle must be blown down into the main stream shock layer behind the bow shock. The critical total pressure ratio to satisfy this starting condition is determined for a combination of free stream and opposing jet exit Mach numbers. When both Mach numbers are equal to 2.81, the critical pressure ratio is 1.177. It can be shown that all the cases calculated satisfy this condition. Therefore the calculated flow field can be regarded to represent the real physical phenomena of the inviscid time-dependent flow. In cases A and D, a disc-like normal shock wave called "Mach disc" appears in front of the nozzle exit as soon as the jet is exhausted from the nozzle at start. Mach disc moves forward with nearly constant speed and also does the bow shock in the main stream. The speed becomes slow for the low total pressure ratio case. The computing mesh was coarse compared with the scale of the region between the bow shock and the Mach disc. Therefore it was not sufficient to get the fine structure of the flow field in this region. Continuity of pressure and discontinuities of density and internal energy across the interface, however, were obtained distinctly as shown in Fig. 10(a) and (b). The average surface pressure on the front side of the body decreased rapidly and became lower than the jet exit static pressure in a short time. The lower the total pressure ratio becomes, the more the time is required for the jet to become underexpanded jet. The pressure continued decreasing until the flow became nearly steady. A vortex appeared in the vicinity of the edge of nozzle exit when the jet started and soon it expanded over the front surface as the jet expansion pushed it outward. The vortex is formed due to the presence of the artificial viscosity because shear stress becomes large at the edge of nozzle exit when the jet stream flows into the stagnant shock layer. The process will be similar in the case of real fluid flow. The bow shock and the Mach disc gradually stop moving forward at about time $t^*=6$, then moving back a little, they become almost at rest as shown in Fig. 17. The motion of the interface is almost the same, it, however, exhibits slow and large oscillation until later time. Because of this, the shape of the interface sometimes becomes concave near the axis as shown in Fig. 10(d). Such remaining unsteadiness is confined in the stagnation region and tends to decay slowly. The change of flow pattern with time becomes almost negligible at about time $t^*=10$ except for the interface region.

*5.2.2. The flow field of steady type*

The contour maps, the streamline plots and the velocity vector plots in Figs. 10, 11 and 16 represent the asymptotic steady flow field of cases A and D. The steady flow pattern can be interpreted from those figures. The jet exit static pressure is well above the surrounding external pressure and the jet flow is accerelated by expansion to form an exhaust plume similar to the one formed by a jet

blown into still air. The jet is decerelated suddenly at the Mach disc. Total pressure losses occur at the Mach disc in the jet stream and at the bow shock in the main stream, respectively, to balance with each other at the interface. Rarefaction waves originate from the nozzle edge and they are reflected along the jet boundary to form a weak intercepting shock wave, the presence of which can be identified by the change of local Mach number, pressure and flow direction although not so obvious. A strong reflected shock appears from the intersecting point of the Mach disc and the intercepting shock. The outer edge of the reflected shock coincides with the jet boundary line calculated from the jet mass flux rate. Although we used the term "Mach disc", it is almost semi-spherically shaped in contrast with the plane Mach disc formed in the underexpanded free jet into still air. The radius of curvature of Mach disc $R_{CMD}/R_j$ is about 3.45 in case A. The shape of the interface is also semi-sphere except the oscillating part near the axis. Neglecting this part, the stand-off distance of the interface from the body $\delta_i/R_b$ is about 2.90~2.95 in case A. The shock layer of the main stream is quite similar to the one around a blunt body. It seems reasonable to replace the interface with solid blunt body of same shape. The radius $R_{CIF}$ of the equivalent blunt body and the radius of curvature $R_{CBS}$ of the bow shock were calculated from the equivalent shock stand-off distance $\Delta_s(=\delta_s-\delta_i)$ using the empirical formula of Ambrosio and Wortman [*55*] for sphere as follows

$$\Delta_s/R_b=0.68\sim0.73, \qquad R_{CIF}/R_b=3.17\sim3.40,$$
$$R_{CBS}/R_b=4.74\sim5.80 \qquad \text{for case } A.$$

The agreement between these values and the plotted shapes of the bow shock and the interface in the figures is fairly good. The shape of sonic line resembles the one around sphere at Mach number range of 2 to 3 as pointed out by Hayes and Probstein [*58*]. Shock jumps and stagnant values on the stagnation streamline are compared with the theoretical ones on Table 3. The relative error is less than 4 per cent except for the pressure in front of Mach disc, of which error is due to the artificial diffusion of shock transition and the influence of reflective boundary condition on the symmetric axis.

TABLE 3. Calculated values at the particular points on the stagnation streamline, case A, $t^*=10$.

| | Behind Bow Shock | Interface | Behind Mach Disc | Before Mach Disc |
|---|---|---|---|---|
| Pressure | 9.0 (9.0455) | 10.4 (10.6415) | 9.8 (9.4271) | 0.45 (0.3660) |
| Density | 3.55 (3.6737) | 4.05 (4.125) | 3.7 (3.7838) | 0.8 (0.7725) |
| Mach Number | 0.50 (0.4875) | — — | 0.50 (0.4197) | 4.62 (4.7137) |

( ) Theoretical value using *R-H* relation and isentropic flow condition

The relation between the stand-off distances and the total pressure ratio gives a good agreement with the experiment of Hayman, et al. as shown in Fig. 19, considering the difference of aerodynamic parameters. The calculated flow pattern also agrees with their photographs. Although the average surface pressure coefficient $C_{pw}$ on the body front surface is slowly oscillating, its mean value, $-0.09$, of case A is very close to the measured value, $-0.08$, by Hayman. The present calculation gives $-0.045$ as the side pressure coefficient while his experiment gives $-0.05$ to $-0.06$. From these comparison, it can be said that FLIC calculation gives good approximation to the surface pressure as well as the flow pattern in spite of the method not taking into account the real viscous effect and the viscous effect being predominant in this region as indicated by the appearance of large vortex. This can be explained as follows. The artificial viscosity terms included in the difference scheme play the qualitatively similar role as the real one. Although the vortex itself is a product of viscosity, its motion is governed mainly by the inviscid flow surrounding the vortex and the effect of difference of the forms between the artificial and real viscosity terms becomes only secondary.

The jet stream decelerated to subsonic speed either by Mach disc or reflected shock flows along the interface turning its direction to downstream and expands again to supersonic speed impinging upon the side surface of the body with an angle of about 20 degrees. "Reattached shock wave" appears in the vicinity of the body shoulder which turns the flow direction to downstream. The corner of the body becomes a stagnation point and the shock wave is detached a little bit from the body surface. When total pressure ratio is high, subsonic region upon the side surface extends to the downstream boundary although it is confined in a thin layer. The presence of strong reattached shock seems to cause such phenomena.

### *5.2.3. Comparison of cases A and B*

As mentioned above, the influence of downstream boundary condition propagates upstream through the subsonic layer upon the body surface and this may cause the change of the pressure in the vortex region which have significant effect on the shape of jet exhaust plume. Another deteriorating influence from the upper-side boundary condition propagates along Mach line which originates from the intersection of the bow shock and the boundary and reaches to the subsonic vortex. To study these problems, case B was calculated in which the computing region was extended to $x^*=+4$ in axial direction and to $r^*=5$ in radial direction. We were compelled to sacrifice the accuracy of solution by making cell size twice of that in case A, because of the insufficient computer memory. The bow shock intersects the upper boundary far behind the front side of the body in case B and the local Mach number there is 2.4 as shown in Fig. 12. Therefore the area affected by the boundary condition is limited to the vicinity of the upper boundary. At the downstream boundary the flow recovers supersonic speed and the effect of the boundary will not propagate upstream. Compared with case A, the time history and asymptotic steady value of the average surface pressure (Fig. 18)

becomes almost same. Shapes and positions of the bow shock, the Mach disc and the sonic line and the distribution of the flow variables also can be regarded the same with case A when we take into account of the coarser mesh (Fig. 10(b), and 12). It may be concluded from the above comparison that the boundary conditions of case A have no significant deteriorating influence upon the numerical solution.

*5.2.4. The flow field of unsteady type*

Another different type of flow field was obtained in case C, in which the nozzle to body radius ratio $R_j/R_b$ was 0.25, the total pressure ratio $p_{0j}/p_{0\infty}$ was 2 and the free stream and jet exit Mach numbers $M_\infty$ and $M_j$ were both 3.00. Strong Mach disc was not formed in the jet stream. The bow shock wave began to move forward from the front face of the body with nearly constant speed when the flow was impulsively started. It seemed to keep moving forward all the time as shown in Fig. 17 while the bow shock stopped at about time $t^*=6$ in the other cases.

When the jet starts, the surface pressure at the front side of the body is much higher than the jet exit static pressure and yet the opposing jet starting condition is satisfied, supersonic jet accompanied by oblique shock from the nozzle edge is formed. The oblique shock is weaken as the jet stream pushes itself into the main stream. A vortex appears from the start as in the steady type (shown in the serial plots in Fig. 15). Since the nozzle exit radius is small in the present case, the vortex is confined in the vicinity of nozzle exit. It takes some time for the vortex to extend all over the front surface. Therefore the average surface pressure decreases slowly compared with the former cases. The asymptotic equilibrium pressure was 0.117 in the unit of pressure coefficient which was slightly lower than the jet exit pressure 0.1588. The nozzle radius was represented by only five cells and the computing mesh was not fine enough to investigate the details of the flow pattern such as the structure of the jet stream and the stagnant region between the bow shock and the jet stream. The contour maps at various times (Fig. 13 and 14) indicate that the stagnant region is confined in a small region of the width of about 0.6 $R_b$ and its structure does not change with time as the jet keeps moving forward. The pressure jump at the bow shock was close to the theoretical value 14.45 which R-H relation gives for the shock Mach number of 3.54. Here the shock Mach number was calculated from the inclination of the curve in Fig. 17.

The periodic pattern of shock waves and rarefaction waves was established in the jet stream soon after the jet started and was left behind the head of the jet. No external boundary condition have any influence on the formation of such wave pattern, because it is established long before any disturbance from the upper boundary reaches the vortex or the body along Mach line (see Fig. 13(f)) and local Mach number at the downstream boundary is supersonic throughout the computation. When the radial width of the computing region was decreased at time $t^*=9$, no abrupt changes of the flow pattern and aerodynamic characteristics such as the surface pressure was observed and the periodic wave pattern continued until the last computing time $t^*=12$. Therefore this flow pattern seems to arise

from the particular aerodynamic conditions applied. It will continue at least until the jet total pressure losses by shocks and artificial viscous dissipation will balance with the main stream total pressure loss at the bow shock.

Romeo and Sterrett observed in their experiments that the bow shock was removed far from the body in a certain range of total pressure ratio. The large shock displacement collapses momentarily and the strong shock pattern like case A appears and then returns to its position far ahead of the body. The unsteadiness is also characterized by irregular oscillation in lateral direction. They explain that the jet flow cannot expand sufficiently so the pressure balance with the main stream by total pressure loss at a normal shock does not occur, and viscous dissipation by mixing process is required to reduce the kinetic energy and to balance with the main stream in this case. There are a number of factors which can cause deviation between theory and experiment such as three-dimensionality, nonuniformity, effect of real viscosity and the like, the results of the present calculation may not be directly compared with the experiments. The process of the formation of the flow pattern obtained in case C, however, seems to show remarkable similarity with the experiment by Romeo and Sterrett. The axial oscillation of the bow shock wave was not obtained in the present calculation. This is because the calculation time corresponds to a very short time of the order of millisecond when transformed to real physical time. It may be regarded the present result as only a part of unsteady solution.

*5.2.5. On the parameters to determine the type of flow field*

It is determined by the selection of aerodynamic parameters and initial condition which type of the flow field is obtained in the calculation. Compareing case C with case D, the initial condition is not same. The former used the impulsive start condition and the latter used steady blunt body flow solution. Time history of the average surface pressure in Fig. 18, however, indicates that the pressure decreases at first and then becomes near-equilibrium for a while soon after the start and again begins to decrase in case C. The velocity plots of this intermediate equilibrium state at time $t^*=1.0$ to 1.5 shows that the vortex is still confined in the vicinity of nozzle exit and the flow pattern outside of the vortex is very like the flow without jet. It is conjectured that the unsteady type of the solution will be obtained in case C even if the blunt body flow solution is applied as the initial condition, although the practical computation will prove it.

The other factors are the aerodynamic parameters, the Mach number of the free stream $M_\infty$ and of the jet $M_j$ and the nozzle to body radius ratio $R_j/R_b$. Total pressure ratio $p_{0j}/p_{0\infty}$ was two in both cases. The magnitude of shear stress and strength of vortex will be represented by a numerical Reynolds number $R_N$ defined by velocity $u_j$, density $\rho_j$, nozzil exit radius $R_j$ and the coefficient of truncation error terms $\varepsilon_x$, which reduces to $(2R_j/\delta x)$. So the numerical Reynolds number is not a function of the flow variables and it merely represents how fine the computing mesh describes the shape of body and the structure of flow field. In the present calculation the numerical Reynolds number does not differ so much be-

tween the both cases and will not have a little influence on the formation of the flow field. The flow Mach numbers also do not differ so much to cause the formation of different flow type. Hayman obtained the steady type of the flow field in experiment in the same range of Mach numbers as the present cases at the total pressure ratio above 2.6. Considering these points, it is conjectured that cases C and D lie near the critical transitional zone where a little deviation of Mach number, nozzle to body radius ratio or total pressure ratio changes the type of the flow field. The critical point for a particular parameter will be determined if numbers of cases are computed by changing the parameter. However, such calculation is not an efficient way of analysis in present days and the obtained result will not give the exact critical value for the parameter found in the experiments because of many a factor different from the experiments.

## 6. Concluding Remarks

To conclude the present study it was shown that the aerodynamic problems containing highly complicated time-dependent and asymptotic steady flow field are numerically obtained by applying one of the computer experiment methods known as the Fluid-in-Cell method: (1) supersonic flow past a circular cylinder perpendicular to the main stream, (2) supersonic flow around a flat-faced circular cylinder parallel to the main stream, and (3) supersonic flow around a flat-faced circular cylinder with a supersonic opposing jet from the nose.

The time asymptotic behaviour and the steady flow field obtained in cases (1) and (2) show close agreement with those of the existing theories and experiments. It was also shown that the FLIC method was extended to the plane polar coordinate system in case (1) and the extension proved to be practical as well as the existing method in the other coordinate systems. The method will be similarly extended to the spherical polar coordinate system.

In case (3), the existing method was applied to the opposing jet problem and it becomes clear that the method can produce sufficient informations to investigate such highly complicated flow field. The calculation shows that two different types of flow field appear according to the governing parameters given as the boundary conditions such as free stream and jet exit Mach numbers, nozzle to body radius ratio and total pressure ratio of the jet to the free stream. One type is a steady flow field with a Mach disc in the jet stream and a bow shock similar to the one in front of a blunt body in the supersonic flow. The other is an unsteady flow field with ever-forward-moving bow shock and periodic wave pattern in the jet stream. The both types of the flow field agree qualitatively with the ones observed in the experiments. However, only a few number of cases were calculated in the present study and more numerical calculations and detailed investigation will be needed in order to determine the dependence of types on the forementioned parameters.

## Acknowledgement

This work was carried out as the doctoral thesis while the author was a post-graduate student at the Institute of Space and Aeronautical Science, University of Tokyo. He wishes to express his sincere gratitude to Professor R. Kawamura for his helpful advices and encouragement throughout. He also would like to thank Assistant Professor N. Satofuka of Kyoto Technical University for useful discussions and comments. Acknowledgement is also given to Mr. K. Seki and author's colleagues at Kawamura Laboratory for their eager assistances on the preparation of the paper.

The calculation were performed on Hitachi HITAC 5020F at the Data Processing Center of the Institute and a part of graphical reduction of data was also performed at the Computer Center of the National Aerospace Laboratory.

*Department of Aerodynamics*
*Institute of Space and Aeronautical Science*
*University of Tokyo, Tokyo*
*October 1, 1971*

## References

[1] Chu, C. K., ed.: "Computational Fluid Dynamics," AIAA Selected Reprint Series, 4, (1968).
[2] "Symposium on Computer Simulation of Plasma and Many-Body Problems, Williamsburg, Virginia, April 19–21, 1967," NASA SP-153, (1967).
[3] "Proceedings of the WMO/IUGG Symposium on Numerical Weather Prediction in Tokyo, November 26–December 4, 1968," Technical Report No. 67, the Japan Meteorological Agency, (1969).
[4] Richtmyer, R. D. and Morton, K. W.: "Difference Methods for Initial-Value Problems, 2nd ed.," Interscience, New York, (1967).
[5] von Neumann, J. and Richtmyer, R. D.: "A Method for the Numerical Calculation of Hydrodynamic Shocks," J. Applied Physics, **21**, pp. 232–237, (1950).
[6] Ludford, G., Polachek, H. and Seeger, R. J.: "On Unsteady Flow of Compressible Viscous Fluids," J. Applied Physics, **24**, pp. 490–495, (1953).
[7] Lax, P. D.: "Weak Solutions of Nonlinear Hyperbolic Equations and Their Numerical Computation," Comm. Pure Appl. Math., **7**, pp. 159–193, (1954).
[8] Rusanov, V. V.: "The Calculation of the Integration of Non-Stationary Shock Waves and Obstacles," USSR Comp. Math. and Math. Physics, **1**, pp. 267–279, (1961).
[9] Bohachevsky, I. O. and Rubin, E. L.: "A Direct Method for Computation of Non-equilibrium Flows with Detached Shock Waves," AIAA J., **4**, pp. 600–607, (1966).
[10] Bohachevsky, I. O. and Mates, R.: "A Direct Calculation of the Flow about an Axisymmetric Blunt Body at Angle of Attack," AIAA J., **4**, pp. 776–782, (1966).
[11] Lax, P. D. and Wendroff, B.: "Systems of Conservation Laws," Comm. Pure Appl. Math., **13**, pp. 217–237, (1960).
[12] Richtmyer, R. D.: "A Survey of Difference Methods for Nonsteady Fluid Dynamics," Technical Note No. 63–2, National Center for Atmospheric Research, (1962).
[13] Burstein, S. Z.: "High Order Accurate Difference Methods in Hydrodynamics," NONLINEAR PARTIAL DIFFERENTIAL EQUATIONS, W. F. Ames, ed., Academic Press, New York, pp. 279–290, (1967).

[*14*] Rubin, E. L. and Burstein, S. Z.: "Difference Methods for the Inviscid and Viscous Equations of a Compressible Gas," J. Computational Physics, **2**, pp. 178–196, (1967).
[*15*] Lapidus, A.: "A Detached Shock Calculation by Second-Order Finite Differences," J. Computational Physics, **2**, pp. 154–177, (1967).
[*16*] Thommen, H. U.: "Numerical Integration of the Navier-Stokes Equations," Z.A.M.P., **17**, pp. 369–384, (1966).
[*17*] Rusanov, V. V.: "On Difference Schemes of Third Order Accuracy for Nonlinear Hyperbolic Systems," J. Computational Physics, **5**, pp. 507–516, (1970).
[*18*] Burstein, S. Z. and Mirin, A. A.: "Third Order Difference Methods for Hyperbolic Equations," J. Computational Physics, **5**, pp. 547–571, (1970).
[*19*] Evans, M. W. and Harlow, F. H.: "The Particle-in-Cell Method for Hydrodynamic Calculations," LA-2139, Los Alamos Scientific Laboratory, (1957).
[*20*] Amsden, A. A.: "The Particle-in-Cell Method for the Calculation of the Dynamics of Compressible Fluids," LA-3466, Los Alamos Scientific Laboratory, (1966).
[*21*] Daly, B. J., Harlow, F. H. and Welch, J. E.: "Numerical Fluid Dynamics Using the Particle-and-Force Method," LA-3144, Los Alamos Scientific Laboratory, (1965).
[*22*] Gentry, R. A., Martin, R. E. and Daly, B. J.: "An Eulerian Differencing Method for Unsteady Compressible Flow Problems," J. Computational Physics, **1**, pp. 87–118, (1966).
[*23*] Gage, W. R. and Mader, C. L.: "Three-Dimensional Cartesian Particle-in-Cell Calculations," LA-3422, Los Alamos Scientific Laboratory, (1965).
[*24*] Butler, T. D.: "Numerical Solutions of Hypersonic Sharp-Leading-Edge Flows," Physics of Fluids, **10**, pp. 1205–1215, (1967).
[*25*] Harlow, F. H. and Pracht, W. E.: "Formation and Penetration of High Speed Collapse Jets," Physics of Fluids, **9**, pp. 1951–1959, (1966).
[*26*] Rich, M.: "A Method for Eulerian Fluid Dynamics," LAMS-2826, Los Alamos Scientific Laboratory, (1963).
[*27*] Butler, T. D.: "Numerical Calculations of the Transient Loading of Blunt Obstacles by Shocks in Air," AIAA J., **4**, pp. 460–467, (1966).
[*28*] Moretti, G. and Abbett, M.: "A Time-Dependent Computational Method for Blunt Body Flows," AIAA J., 4, pp. 2136–2141, (1966).
[*29*] Masson, B. S., Taylor, T. D. and Foster, R. M.: "Application of Godunov's Method to Blunt-Body Calculations," AIAA J., **7**, pp. 694–698, (1969).
[*30*] Hirose, N.: "Numerical Calculation of Shock Tube Flow by Two-Material Fluid-in-Cell Method," Bulletin of the I.S.A.S., University of Tokyo, **7**, pp. 385–402, (1971).
[*31*] Landshoff, R.: "A Numerical Method for Treating Fluid Flow in the Presence of Shocks," LA-1930, Los Alamos Scientific Laboratory, (1955).
[*32*] Harlow, F. H.: "The Particle-in-Cell Method for Numerical Solution of Problems in Fluid Dynamics," Proc. Symp. Appl. Math., Vol. 15, A.M.S., pp. 269–288, (1963).
[*33*] Burstein, S. Z.: "Finite Difference Calculations for Hydrodynamic Flows Containing Discontinuities," J. Computational Physics, **1**, pp. 198–222, (1966).
[*34*] Kaplan, M. A. and Papetti, R. A.: "An Analysis of the Two-Dimensional Particle-in-Cell Method," RM-4876-PR, The RAND Corporation, (1964).
[*35*] Courant, R., Friedrichs, K. O. und Lewy, H.: "Über die partiellen Differenzengleichungen der mathematischen Physik," Mathematische Annalen, **100**, pp. 32–74, (1928).
[*36*] Van Dyke, M. D.: "The Supersonic Blunt-Body Problem - Review and Extension," J. Aeronautical Sciences, **25**, pp. 485–496, (1958).
[*37*] Vaglio-Laurin, R. and Ferri, A.: "Theoretical Investigation of the Flow Field about Blunt-Nosed Bodies in Supersonic Flight," J. Aeronautical Sciences, **25**, pp. 761–770, (1958).
[*38*] Fuller, F. B.: "Numerical Solutions for Supersonic Flow of an Ideal Gas Around Blunt Two-Dimensional Bodies," NASA TN D-791, (1961).
[*39*] Lomax, H. and Inouye, M.: "Numerical Analysis of Flow Properties About Blunt Bodies Moving at Supersonic Speeds in an Equilibrium Gas," NASA TR R-204, (1964).
[*40*] Swigart, R. J.: "Hypersonic Blunt-Body Flow Fields at Angle of Attack," AIAA J.,

2, pp. 115–117, (1964).
[41] Hamaker, F. M.: "Numerical Solution of the Flow of a Perfect Gas Over a Circular Cylinder at Infinite Mach Number," NASA Memorandum 2-25-59A, (1959).
[42] Uchida, S. and Yasuhara, M.: "The Rotational Field Behind a Curved Shock Wave Calculated by the Method of Flux Analysis," J. Aeronautical Sciences, **23**, pp. 830–845, (1956).
[43] Belotserkovskii, O. M., ed.: "Supersonic Gas Flow Around Blunt Bodies, Theoretical and Experimental Investigations," NASA TT F-453, (1967).
[44] Moretti, G.: "Inviscid Blunt Body Shock Layers—Two-Dimensional Symmetric and Axisymmetric Flows," PIBAL No. 68–15, Polytechnic Institute of Brooklyn, New York, (also on AD-672543), (1968).
[45] Kendal, Jr., J. M.: "Experiments on Supersonic Blunt-Body Flows," J.P.L. Progress Report No. 20–372, Jet Propulsion Laboratory, (1959).
[46] South, Jr., J. C.: "Calculation of Axisymmetric Supersonic Flow Past Blunt Bodies with Sonic Corners, Including a Program Description and Listing," NASA TN D-4563, (1968).
[47] Watt, G. A.: "An Experimental Investigation of a Sonic Jet Directed Upstream Against a Uniform Supersonic Flow," Technical Note No. 7, Institute of Aerophysics, Univ. of Tront, (1956).
[48] Charczenko, N. and Hennessey, K. W.: "Investigation of a Retrorocket Exhausting from the Nose of a Blunt Body into a Supersonic Free Stream," NASA TN D-751, (1961).
[49] Hayman, L. O. and McDearmon, R. W.: "Jet Effects on Cylindrical Afterbodies Housing Sonic and Supersonic Nozzles Which Exhaust Against a Supersonic Stream at Attack from 90° to 180°," NASA TN D-1016, (1962).
[50] Romeo, D. J. and Sterrett, J. R.: "Exploratory Investigation of the Effect of a Forward-Facing Jet on the Bow Shock of a Blunt Body in a Mach Number 6 Free Stream," NASA TN D-1605, (1963).
[51] Cassanova, R. A. and Wu, Y. C. L.: "Flow Field of a Sonic Jet Exhausting Counter to a Low-Density Supersonic Airstream," Physics of Fluids, **12**, pp. 2511–2514, (1969).
[52] Taylor, T. D. and Masson, B. S.: "Supersonic Flow Past Blunt Bodies with Large Surface Injection," IAF Paper RE-42, (1968).
[53] Miles, J. W., Mirels, H. and Wang, H. E.: "Time Required for Establishing Detached Bow Shock," AIAA J., **4**, pp. 1127–1128, (1966).
[54] Kim, C. S.: "Experimental Studies of Supersonic Flow Past a Circular Cylinder," J. Physical Society of Japan, **11**, pp. 439–445, (1956).
[55] Ambrosio, A. and Wortman, A.: "Stagnation Point Detachment Distance for Flow Around Spheres and Cylinders," ARS J., **32**, pp. 281, (1962).
[56] Moretti, G.: "The Importance of Boundary Conditions in the Numerical Treatment of Hyperbolic Equations," PIBAL No. 68–34, Polytechnic Institute of Brooklyn, New York, (also on AD-681365), (1968).
[57] Houghton, D., Kasahara, A. and Washington, W.: "Long-Term Integration of the Barotropic Equations by the Lax-Wendroff Method," Monthly Weather Review, **94**, pp. 141–150, (1966).
[58] Hayes, W. D. and Probstein, R.: "Hypersonic Flow Theory, Inviscid Flows, Vol. 1," Appl. Math. Mech. Vol. 5A, Academic Press, New York, Chapter 6, (1966).